coatings

MDPI

Article

Induced Codeposition of Tungsten with Zinc from Aqueous Citrate Electrolytes

Honorata Kazimierczak and Noam Eliaz *

Biomaterials & Corrosion Laboratory, Department of Materials Science and Engineering, Tel-Aviv University, Ramat Aviv, Tel Aviv 6997801, Israel; honorata.kazimierczak@gmail.com
* Correspondence: neliaz@tauex.tau.ac.il

Abstract: Zinc–tungsten coatings have been considered as environmentally friendly, and corrosion- and wear-resistant coatings. Here, Zn–W coatings were successfully electrodeposited from an aqueous solution. Citrate-based electrolytes with pH in the range of 3.0 to 5.7 were used as plating baths. The kinetics of co-reduction in the Zn(II)–W(VI)–Cit system was studied on the basis of partial polarization curves. The effects of applied potential, electrolyte composition, pH, hydrodynamic conditions and passed charge on the electrodeposition of Zn–W layers were determined. X-ray photoelectron spectroscopy confirmed the presence of metallic tungsten co-deposited with zinc. X-ray diffraction analysis revealed the formation of hexagonal Zn–W phase resulting from a substitution of Zn atoms by W atoms in the Zn crystal lattice. The formation of the proper stable and electroactive W(VI) and Zn(II) complexes is the first crucial factor enabling the induced codeposition of Zn–W alloys. The tungsten content in the Zn–W deposit is closely related to the concentration of electroactive tungstate–citrate species and its ratio relative to the zinc–citrate electroactive species in the electrolytic bath. The oxidation state of tungsten in the electrodeposited Zn–W layers can be controlled mainly by the applied deposition potential and by the bath pH, which determines the type of W(VI)–Cit species that can be reduced.

Keywords: zinc; tungsten; citrates; Zn–W alloy; induced codeposition

Citation: Kazimierczak, H.; Eliaz, N. Induced Codeposition of Tungsten with Zinc from Aqueous Citrate Electrolytes. *Coatings* **2023**, *13*, 2001. https://doi.org/10.3390/coatings13122001

Academic Editor: Paweł Nowak

Received: 27 October 2023
Revised: 20 November 2023
Accepted: 22 November 2023
Published: 25 November 2023

1. Introduction

It is commonly known that the addition of tungsten (W) to alloys improves their mechanical properties and corrosion resistance, while posing a significantly lower environmental risk in comparison with either Cr(VI) or nickel- and cobalt-based compounds, which are commonly used as alloying additives in zinc-based protective coatings. Moreover, due to tungsten occurrence at various oxidation states and its strong film-forming abilities on a number of metallic surfaces, it has been proposed as an essential component of new, environmentally benign protective coating systems [1–9].

The preparation of Zn–W alloys by conventional thermal methods is considered impossible because (1) there are big differences in the melting and boiling temperatures of Zn and W (T_m = 419.53 and 3422 °C, respectively; T_b = 907 and 5930 °C, respectively); (2) W cannot form an alloy with Zn, at least at temperatures of up to 1350 °C [10]; (3) W is not wetted by molten Zn [11]; (4) W is highly resistant to corrosion in molten Zn and in Zn vapour [12–14]; (5) neither a W–Zn phase diagram nor binary W–Zn compounds have been reported [12,15].

Electrodeposition, on the other hand, allows the formation of alloys with metastable phases or phases that are either deficient or oversaturated in one of the elements compared to their equilibrium counterpart phases appearing in the thermodynamic phase diagram [9,16–20]. Yet, W (and Mo) cannot be electrodeposited in a pure state from aqueous solutions; the presence of another metal is required for induced codeposition [8,21]. Tungsten codeposition with iron-group metals occurs far more readily than with other

metals; hence, its codeposition with Ni, Fe and Co has been most widely studied since the 1930s [17,21–33]. These alloys have been reported to have attractive mechanical, tribological, magnetic, electrical and electrochemical and corrosion resistance properties [9,21–23,34–37]. Regarding the mechanism of induced codeposition, it has been suggested that the iron-group metals may act as catalysts in the formation of intermediate products [9,31–33]. It is indisputable that this is a complex, multi-step process; it is still not understood well.

Only few reports have been published on the electrochemical codeposition of W from aqueous solutions with elements other than iron-group metals. Holt [26] studied the effect of a number of metals on W codeposition, using a simple plating bath based on sodium carbonate and tungstic acid, with a small addition of salts of the other metals. It was argued that, except for the three iron-group metals, only tin and cadmium codeposited with W, forming an alloy. These Sn–W and Cd–W deposits were described as shiny metallic and silvery, respectively. Rogers and Burr [38] studied Cr–W electrodeposition from solution of chromic acid, ammonium citrate and tungsten trioxide, and reported 28%–36% W in the coating. Clark and Lietzke [39] hypothesized that W–Mn and W–Cu codeposition may follow a similar mechanism of codeposition as W–Fe, W–Co, W–Ni and W–Cr since they are neighboring elements in the periodic table. W–Mn and W–Cu codeposition was thus studied from aqueous citrate–ammonia baths containing sodium tungstate and either Mn- or Cu-sulfate. The coatings obtained this way were metallic in appearance, adherent to the substrate, and contained either 14% or 2% W in Mn–W and Cu–W layers, respectively. The formation of tungstate–citrate complexes was suggested essential for the codeposition of metallic tungsten. Unfortunately, detailed characterization of the deposits was not provided in [26,38,39].

More recently, Bacal et al. [40,41] investigated the codeposition of W with Cu from aqueous citrate solution containing also boric acid and phosphoric acid. The electrodeposition of Cu–W alloy with a tungsten content of up to 30 wt.% was reported. XRD analysis indicated that the alloy consisted of nanometer-sized polycrystalline Cu in an amorphous solid solution of Cu and W. Vernickaite et al. [42] also studied codeposition of W with Cu from aqueous citrate baths. They reported the codeposition of up to 6 at.% W and characterized the microstructure as a solid solution with a Cu-type face-centered cubic (fcc) unit cell. Saito [43] reported Cu–W alloy codeposition with up to 6 wt.% W using aqueous tartrate baths and the pulse-plating process. The abovementioned works neither propose a mechanism of W codeposition with Cu nor study the possible formation of a complex and its influence on the codeposition process.

To date, there is no report available, to the best of our knowledge, on the codeposition of metallic W with Zn without also adding iron-group metals. Nakano et al. [44] studied the electrodeposition of Zn from simple acidic sulphate baths with small amounts of W- and Mo-based oxoacidic salts. However, no codeposition of either W or Mo with Zn was observed. Only some effect on the surface morphology and crystal orientation of Zn deposits was noticed, depending on the presence of the W (and Mo) ions in the electrolyte during the deposition process. Sadjadi et al. [45] tried developing an electroless deposition process of Zn–W–B alloy using dimethyl amine borane (DMAB) as a reducing agent, and cetyltrimethylammonium ammonium bromide (CTAB) as a complexing agent, in an aqueous bath with zinc sulphate and sodium tungstate as metal sources. Nevertheless, only oxide phases of ZnO and WO_2 were identified in the deposits by XRD.

Kazimierczak et al. [46–48] showed that Zn can induce codeposition of metallic Mo from citrate electrolytes, without addition of iron-group metals that had been claimed necessary before [9,49]. It was claimed that the formation of a mixed Zn(II)–Mo(VI)–Cit complex via the subsequent adsorption of Zn(II)–Cit and Mo(VI)–Cit complexes on the cathode surface allows its further reduction to Zn–Mo alloy [47]. Thick Zn–Mo layers containing 0.5 to 50 wt.% Mo were obtained, and XPS analysis confirmed the presence of metallic Mo in the electrodeposited layers. Addition of small amounts of Mo (0.5 to 1.5 wt.%) to Zn was found optimal for the decrease in surface roughness, increase in microhardness,

and improvement of the corrosion resistance in chloride solutions compared to pure Zn layers [47,50–52].

Citrates are known to form strong complexes with both Zn(II) and W(VI); moreover, they are non-toxic and provide electrolyte pH stabilization [53–56]. Therefore, in this work, aqueous citrate solutions are proposed as electroplating baths for the codeposition of Zn with W. The objectives of the work are (i) to develop stable citrate aqueous baths containing Zn(II) and W(VI) ions in the form of electroactive complex species; (ii) to analyze the kinetics and mechanism of co-reduction of Zn(II) and W(VI) from these baths; and (iii) to characterize the electrodeposited Zn–W alloy layers.

2. Materials and Methods

To analyze the stability of the Zn(II)–W(VI)–citrate system, a thermodynamic model of species distribution was made based on the stability constants of the species [57–59]. The calculations were made using HYDRA and MEDUSA programs [60].

Sodium citrate, $C_6H_5Na_3O_7{\cdot}2H_2O$, is denoted herein as Na_3HCit, where Cit denotes $C_6H_4O_7$. In the literature, two different designations of citrate ion can be found, Cit^{4-} and Cit^{3-} [61,62]; the former is used hereafter. Thus, Cit^{4-} implies $C_6H_4O_7{}^{4-}$, i.e., the deprotonated form of acid radical of sodium citrate [63]. The electrolyte solutions were prepared by dissolving sodium citrate (0.10–0.60 M), zinc sulphate (0.1–0.3 M) and sodium tungstate (0.05–0.40 M) in deionized (DI) water. The solution pH was adjusted by adding sulfuric acid or sodium hydroxide. All chemicals used were of analytical grade. All electrochemical measurements were carried out in a 150 cm^3 cell, at ambient temperature (ca. 25 °C), in a system with a rotating disc electrode (RDE) to ensure constant and controlled hydrodynamic conditions. The working electrode was a copper disc placed in a sealed Teflon holder (active surface area of 0.07 cm^2). A platinum sheet (2 cm^2) was used as a counter electrode. All potentials were measured versus a saturated calomel electrode (SCE). The measurements were performed potentiostatically in a three–electrode cell, using an Ametek ParSTAT263A potentiostat/galvanostat.

The faradaic efficiency (FE, also known as current efficiency) of the electrodeposition processes and the partial polarisation curves were determined on the basis of the chemical composition of the deposits (as determined by energy dispersive X-ray spectrometry, EDS), the passed charge, and the deposited mass, assuming that W(VI) is reduced on the electrode to W. The samples were weighed before and after the deposition process using Precisa ES 225SM analytical scales with a readability of 0.01 mg. The reproducibility of the electrodeposition process was verified using three to five replicates; typical results are reported herein. The values of current density are presented in accordance with the IUPAC convention (the increase or decrease in current density value discussed hereafter refers to its absolute value).

The surface morphology of the deposited layers was characterized by means of a scanning electron microscope (ESEM, Quanta 200 FEG from FEI, Hillsborough, OR, USA) operated in the high-vacuum mode. The attached Oxford Si EDS detector was used to determine the chemical composition of the electrodeposited alloy. The whole surface of each sample was analyzed five to ten times (samples with higher surface roughness were analyzed more times), giving the average value and standard deviation of the W-content.

The oxidation states of elements in the alloy were determined by XPS. XPS measurements were performed in UHV (2.5×10^{-10} Torr base pressure) using 5600 Multi–Technique System (Physical Electronics, Inc. (PHI), Chanhassen, MN, USA). The sample was irradiated with an Al K_α monochromated source (1486.6 eV), and the outcome electrons were analyzed by a Spherical Capacitor Analyzer using a slit aperture of 0.8 mm. The samples were analyzed at the surface and after sputter cleaning (sputter rate was 47.6 Å/min on SiO_2/Si reference sample). The sputtering time was set as the time needed to remove most of the organic contamination from the surface without destroying the chemical bonds on the surface. Tungsten oxide can be reduced into several oxidation states when sputtered, making the minimal sputtering time preferable. Depth profiling was used to determine

the optimal sputtering time. It was observed that, after 0.5 min of sputtering, the carbon peak intensity dropped by approximately an order of magnitude. After 1 min of sputtering, tungsten oxides were either reduced or removed, while, after 0.5 min, neither significant reduction nor removal was observed. Hence, 0.5 min sputtering was used in all sample analyses. Sample charging was compensated with a charge Neutralizer, as needed. XRD measurements were performed using a Bruker D8 DISCOVER diffractometer with a Cu Kα radiation source in theta/theta scan with parallel beam for phase identification.

3. Results and Discussion

3.1. Development of Stable Baths for Electrodeposition of Zn–W Alloys

The preparation of stable solutions is one of the basic problems in the development of new alloy electrodeposition. The type of complexes formed in aqueous citrate solutions depends on pH, concentration of components and temperature. It was stated in our previous studies that, in the case of Zn-based alloy deposition, the concentration of sodium citrate in the electrolyte solution should be equal to, or slightly higher than, the concentration of the deposited metal ions [47,56]. Hence, a bath containing 0.30 M Na_3HCit, 0.20 M $ZnSO_4$ and 0.10 M Na_2WO_4 was proposed as the starting point in this work. According to the thermodynamic model (Figure 1), stable and electroactive complexes of Zn(II) and W(VI) are expected to be present in the solution simultaneously, as main ions, in a relatively wide pH range between ca. 2 and 6. Although the ZnH_2Cit^0 and Zn_2Cit^0 complexes are known to form sparingly soluble polymers, they are electroactive and can be considered stable for several weeks, only after which precipitates gradually start forming [56,64]. At a pH higher than 6, the dominant Zn(II) species are $ZnH_2Cit_2^{4-}$ and $Zn_2Cit_2^{4-}$ which, despite being homogeneous, are known to be non–electroactive because of their high electronegativity [56,65]. In this work, plating baths with a pH range from 3.0 to 5.7 were used for up to four weeks after their preparation, yet no precipitates were observed. Consequently, three pH values were chosen for further study: pH = 3.0, 4.3 and 5.7, at which the highest concentration of different tungstate–citrate complexes are expected to be present together with electroactive Zn–citrate ions (Figure 1). The chosen pH values ensure a relatively low rate of hydrogen evolution, since the concentration of H_3Cit^- ions is very low at pH = 3, whereas there are effectively no free citrate ions at pH = 5.7.

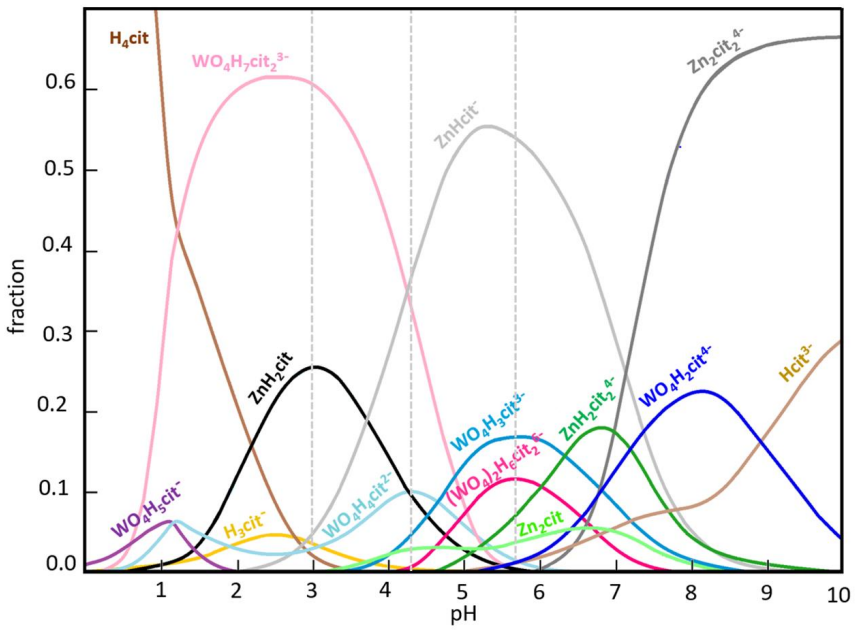

Figure 1. The distribution of species in the Zn–W–Cit system as a function of pH of a solution containing 0.30 M Na_3HCit, 0.20 M $ZnSO_4$ and 0.10 M Na_2WO_4. The gray dotted line marks the pH of the solutions used in this work.

3.2. Steady-State Behavior

The steady-state partial polarization curves of co-discharge of Zn(II), W(VI) and hydrogen are drawn in Figure 2a_1–a_5, in comparison with the dependence of both the W-content in the deposit (Figure 2b) and the faradaic efficiency of the applied deposition potential (Figure 2c). It is evident that, for all three pH values, the codeposition of W with Zn (Figure 2a_3–a_5) takes place within the whole range of applied potential, i.e., from −1.15 V vs. SCE to −1.75 V vs. SCE.

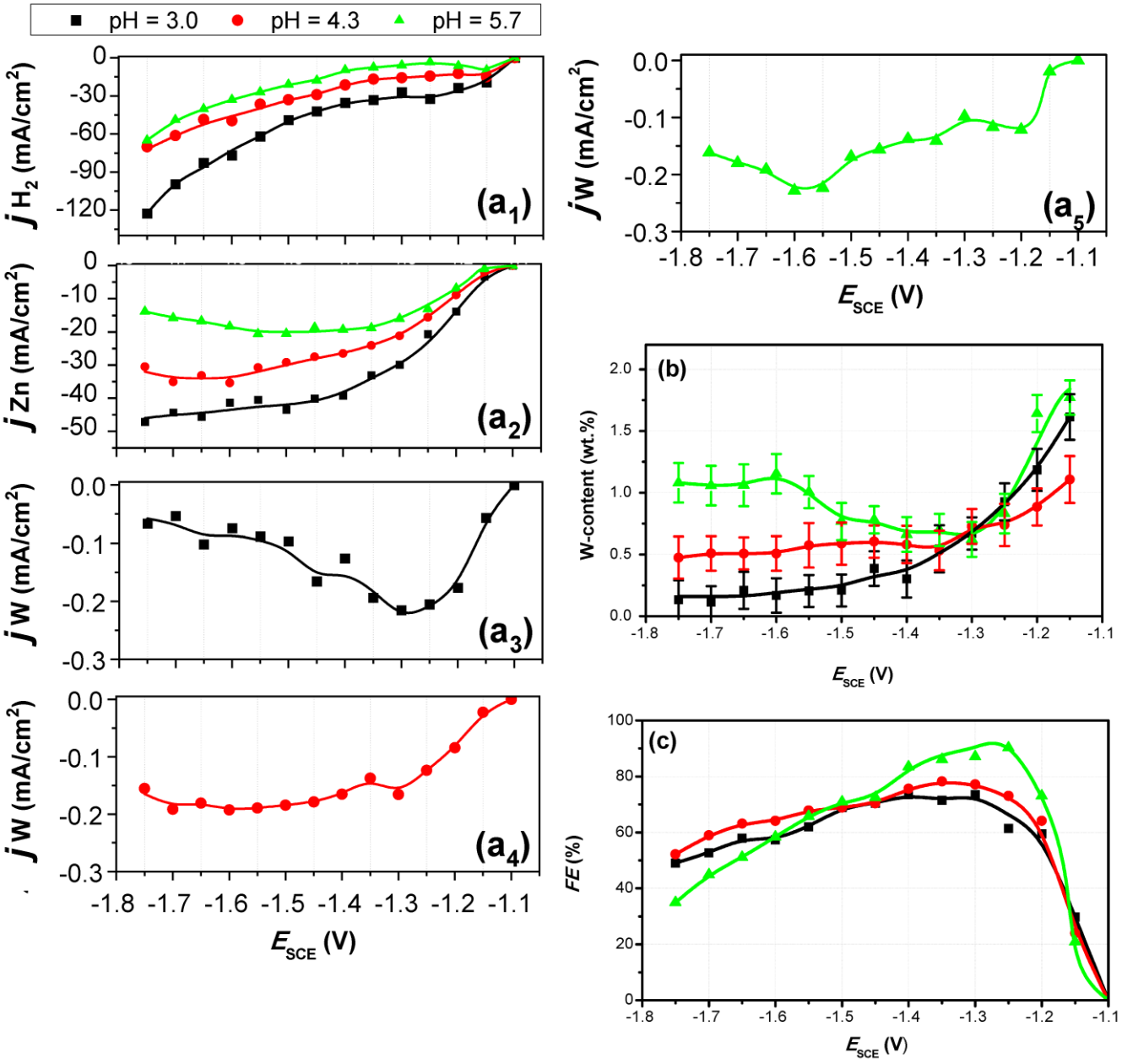

Figure 2. Steady-state partial polarization curves of hydrogen (**a_1**), zinc (**a_2**) and tungsten (**a_3–a_5**) codeposition. (**b**) W-content in Zn–W deposit as a function of the potential of the working electrode. (**c**) The dependence of faradaic efficiency on the potential of the working electrode. The electrolyte consisted of 0.30 M Na_3HCit, 0.20 M $ZnSO_4$ and 0.10 M Na_2WO_4; pH = 3.0, 4.3, or 5.7. ω = 250 rpm, Q = 20 C/cm^2, T = 25 °C, Cu substrate. The average and standard deviation values of W-content in the coating are noted in (**b**).

In the case of electrodeposition from a bath with pH = 3.0, the partial current of tungsten reduction has a clear maximum at a potential of ca. −1.3 V vs. SCE (Figure 2a$_3$). Further shift toward more negative potentials results in a gradual decrease in tungsten deposition rate along with a slight increase in zinc deposition rate (Figure 2a$_2$) and a noticeably greater increase in the hydrogen evolution rate (Figure 2a$_1$). The zinc partial current is highest at pH = 3.0 (compared with the other two pH values), thus confirming that the ZnH_2Cit^0 complex is electroactive; since it is neutral, it is easier to reduce it to metallic form compared to $ZnHCit^-$ complex, which is the dominant zinc species at pH = 5.7 (see Figures 1 and 2a$_2$). The relatively high partial current of hydrogen evolution at pH = 3.0 is related to the presence of H_3Cit^- (see Figure 1), which is reduced to H_2, along with the H_2Cit^{2-} ions that are the by-product of ZnH_2Cit^0 ions' reduction to Zn [56].

The partial polarization curve of tungsten deposition from a bath at pH = 4.3 can be divided into two regimes: after a local maximum of W reduction at E = −1.3 V vs. SCE, a plateau-like regime with a slightly higher cathodic current density is observed in the potential range from ca. −1.45 V to −1.70 V vs. SCE (Figure 2a$_4$). This may be related to the presence of two tungstate–citrate complexes (see Figure 1). The $WO_4H_7Cit_5^{3-}$ fraction is much lower at pH = 4.3 compared to pH = 3.0 (Figure 1), thus the W deposition rate at the first local maximum in a bath with pH = 4.3 is lower compared to the partial W current in the same potential range in a bath with pH = 3.0 (Figure 2a$_3$,a$_4$). On the other hand, the concentration of $WO_4H_4Cit^{2-}$ has a maximum at pH = 4.3 (Figure 1), and the partial current of W deposition is much higher in the higher polarization range, compared to pH = 3.0 (Figure 2a$_3$,a$_4$). This indicates that the higher polarization regime with a current density plateau is related to the co-discharge associated with $WO_4H_4Cit^{2-}$ reduction, while the low-polarization regime, with a local maximum at −1.3 V vs. SCE, is associated with $WO_4H_7Cit_5^{3-}$ discharge.

The rate of Zn deposition is lower at pH = 4.3 compared to pH = 3.0, within the whole range of applied potentials (Figure 2a$_2$). This is correlated with a sharp drop in the fraction of ZnH_2Cit^0 ions and a significant increase in the fraction of the $ZnHCit^-$ complex (Figure 1). Furthermore, the zinc partial polarization curve registered at pH = 5.7 shows even lower rates of Zn deposition compared to the more acidic baths (Figure 2a$_2$). It is thus correlated with the further increase in the fraction of $ZnHCit^-$ ions, which are the dominant electroactive Zn–Cit species under such conditions (Figure 1).

When examining the partial polarization curves of W deposition, the results obtained at pH = 4.3 (Figure 2a$_4$) and at pH = 3.0 (Figure 2a$_3$) show some resemblance. However, in contrast to the partial polarization curve at pH = 5.7 (Figure 2a$_5$), the latter is much different. This is likely related to the fact that different tungstate–citrate species are formed at pH = 5.7 (see Figure 1). Only in the case of deposition from a bath with pH = 5.7 is an increase in W content in the Zn–W deposit in the higher polarization regime (starting at –1.5 V vs. SCE) observed (Figure 2b). Consequently, two local maxima of tungsten deposition rate can be observed (Figure 2a$_5$), which are related to the presence of two complexes: $WO_4H_3Cit^{3-}$ and $(WO_4)_2H_6Cit_2^{6-}$. It may be assumed that the first local maximum at E = −1.20 V vs. SCE is related to the reduction of a less negative complex, $WO_4H_3Cit^{3-}$, while the second local maximum at ca. E = −1.6 V vs. SCE is related to the co-discharge of a more negative complex ion, $(WO_4)_2H_6Cit_2^{6-}$. However, a further in-depth study is required to draw this conclusion unequivocally.

3.3. The Effect of Hydrodynamic Conditions

The effect of RDE speed on the electrodeposition of Zn–W was investigated in electrolytes with the same composition and pH values (Figure 3). The rotation rate of the working disc electrode was varied between 26 and 209 rad/s (250–2000 rpm).

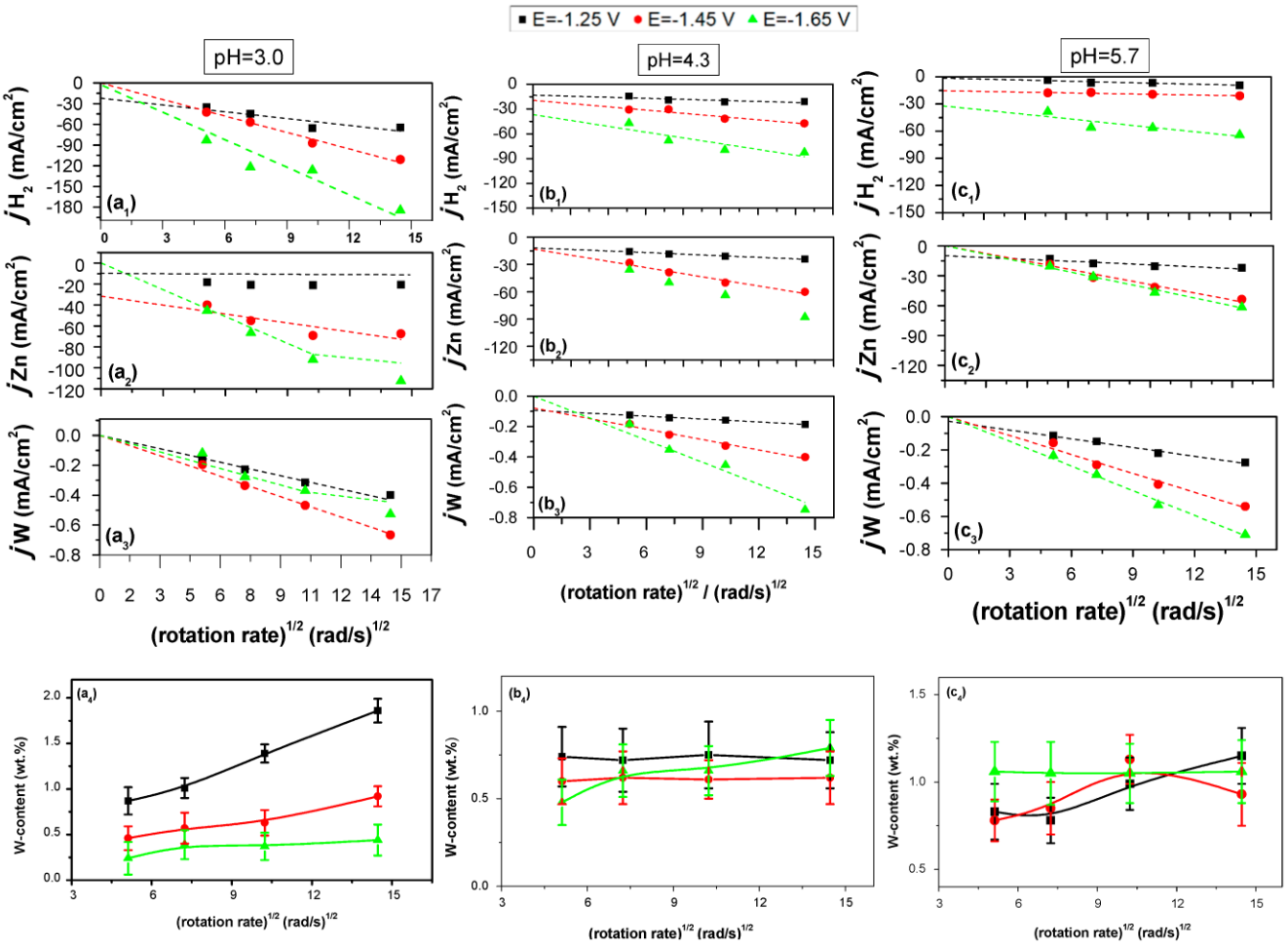

Figure 3. Effect of RDE rate on the electrodeposition process. The partial current densities of hydrogen (**a**$_1$,**b**$_1$,**c**$_1$), Zn (**a**$_2$,**b**$_2$,**c**$_2$) and W (**a**$_3$,**b**$_3$,**c**$_3$) codeposited as a function of RDE speed. (**a**$_4$,**b**$_4$,**c**$_4$) The W-content in the Zn–W deposits as a function of RDE speed at deposition potentials of −1.25 V, −1.45 V and −1.65 V and pH values of 3.0, 4.3, and 5.7. Bath composition: 0.30 M Na_3HCit, 0.20 M $ZnSO_4$, 0.10 M Na_2WO_4. Q = 20 C/cm^2, ω = 250–2000 rpm, T = 25 °C, Cu substrate.

In the case of Zn–W deposition from a bath at pH = 3.0, Zn partial current density is independent of the RDE speed at E = −1.25 V vs. SCE; hence, it is activation-controlled. At more negative potentials (E = −1.45 and −1.65 V vs. SCE), the Zn codeposition processes change to mixed activation–diffusion- and fully diffusion-controlled, respectively (Figure 3a$_2$). On the other hand, at pH = 3.0, the W codeposition process is fully diffusive, with the linear dependence of the W partial current on the square root of the RDE rate passing through the origin of the plot, for all three applied electrode potentials (Figure 3a$_3$). Under such conditions, when activation-controlled Zn codeposition occurs together with diffusion-controlled W codeposition, a linear increase in the W content in the coating is evident, and is mostly visible for E = −1.25 V vs. SCE (from 0.9 ± 0.1 to 1.9 ± 0.1 wt.% W at 250 and 2000 rpm, respectively; see Figure 3a$_4$).

For hydrogen evolution in a bath at pH = 3.0, the kinetics changes from mixed activation–diffusion-controlled at E = −1.25 V vs. SCE to fully diffusion-controlled at more negative deposition potentials (Figure 3a$_1$). The hydrogen evolution rate in this case is much higher than in the cases of depositions at pH = 4.3 (Figure 3b$_1$) or 5.7 (Figure 3c$_1$) due to the higher acidity of this bath and the presence of H_3Cit^- ions. In all cases, no correlation between the kinetic regimes of hydrogen evolution, Zn and W codeposition can be clearly claimed. On the other hand, in a bath at pH = 4.3, the partial currents of both Zn and W deposition exhibit mixed activation–diffusion control at lower polarization (E = −1.25

and −1.45 V vs. SCE) and full diffusion control at E = −1.65 V vs. SCE (Figure 3b_2,b_3). In the case of a bath at pH = 5.7, only codeposition at −1.25 V is mixed kinetically controlled, while higher polarization leads to fully diffusion-controlled Zn and W codeposition (Figure 3c_2,c_3). This results in a relatively constant W content in the deposited Zn–W alloys, ranging from 0.60 ± 0.15 wt.% W (Figure 3b_4) to 0.8 ± 0.2 wt.% W (Figure 3c_4) for baths at pH = 4.3 or 5.7, respectively.

3.4. The Effect of Passed Charge

Next, the dependence of the electrodeposition process on the total passed charge was studied for the same three deposition potentials and same three bath pH values (Figure 4). The value of the passed charge was varied from 20 to 50 C/cm^2, corresponding to deposit thicknesses of ca. 4 μm and 16 μm, respectively. These thickness values were calculated based on coating mass gain measurements, assuming a uniform coating thickness, which was verified by random metallographic cross-section analyses.

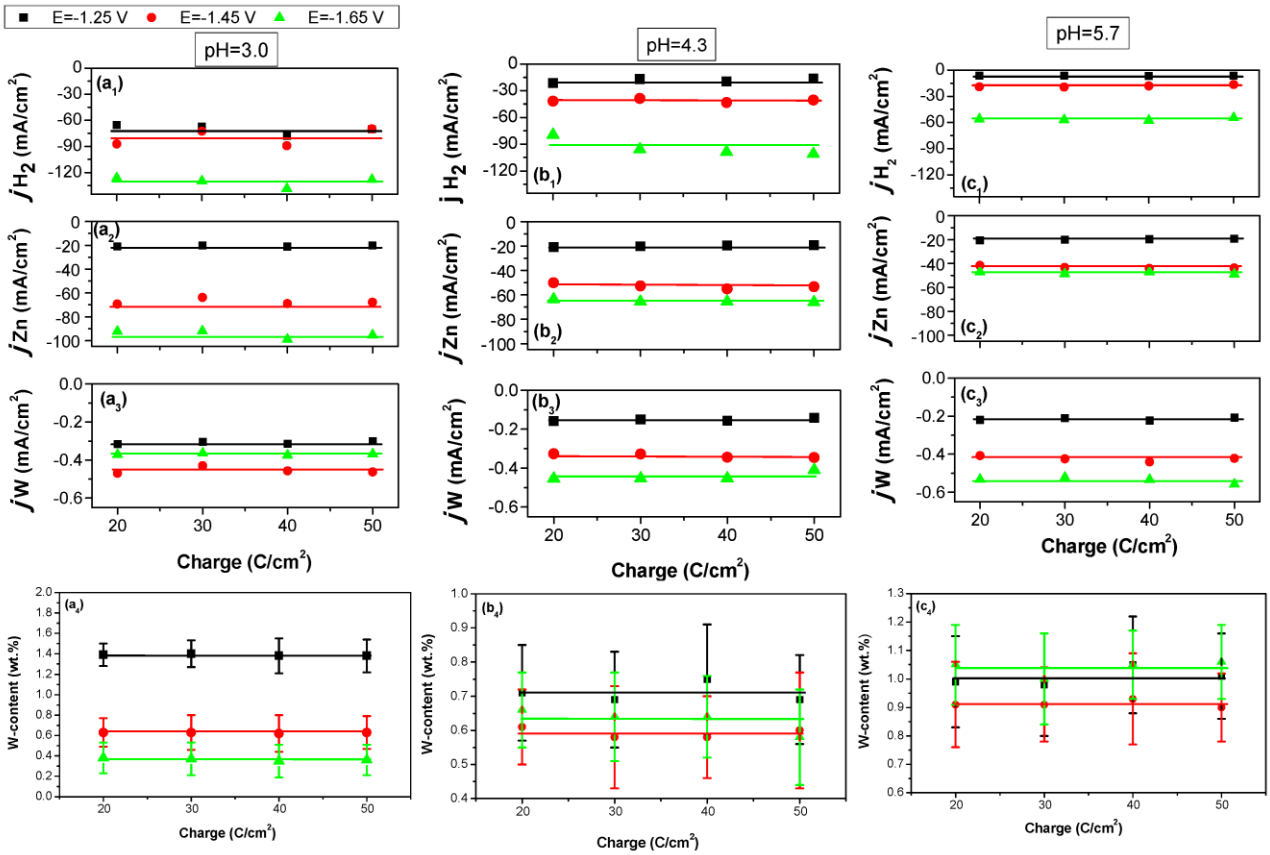

Figure 4. The effect of passed charge on the electrodeposition process. The partial current densities for codeposition of hydrogen (**a_1**,**b_1**,**c_1**), Zn (**a_2**,**b_2**,**c_2**), and W (**a_3**,**b_3**,**c_3**) as a function of total passed charge. (**a_4**,**b_4**,**c_4**) The W-content in Zn–W deposits as a function of total passed charge, for the three deposition potentials and three pH values. Bath composition: 0.30 M Na_3HCit, 0.20 M $ZnSO_4$, 0.10 M Na_2WO_4. ω = 1500 rpm, Q = 20 C/cm^2, T = 25 °C, Cu substrate.

It is evident that the deposition processes are stable through the whole range of applied charge, in all studied cases (Figure 4a_1–c_3). Consequently, the concentration of W is constant through the cross-section of the deposited layers (Figure 4a_4,b_4,c_4). This was confirmed by EDS analysis of coating cross-sections (Figures S1 and S2 in Supplementary Materials). Hence, it can be concluded that our Zn–W deposition process is stable, and that W codeposition proceeds invariably with Zn deposition.

3.5. The Effect of Bath Composition

The effect of sodium tungstate and sodium citrate concentrations in an electrolyte with pH = 5.7 was further studied (Figures 5 and 6). The concentration of Na_2WO_4 was varied from zero to 0.40 M, simultaneously with a respective increase in Na_3HCit concentration, from 0.20 M to 0.60 M, so that all the Zn(II) and W(VI) species were maintained in the plating bath in the form of citrate complexes (Figure 6).

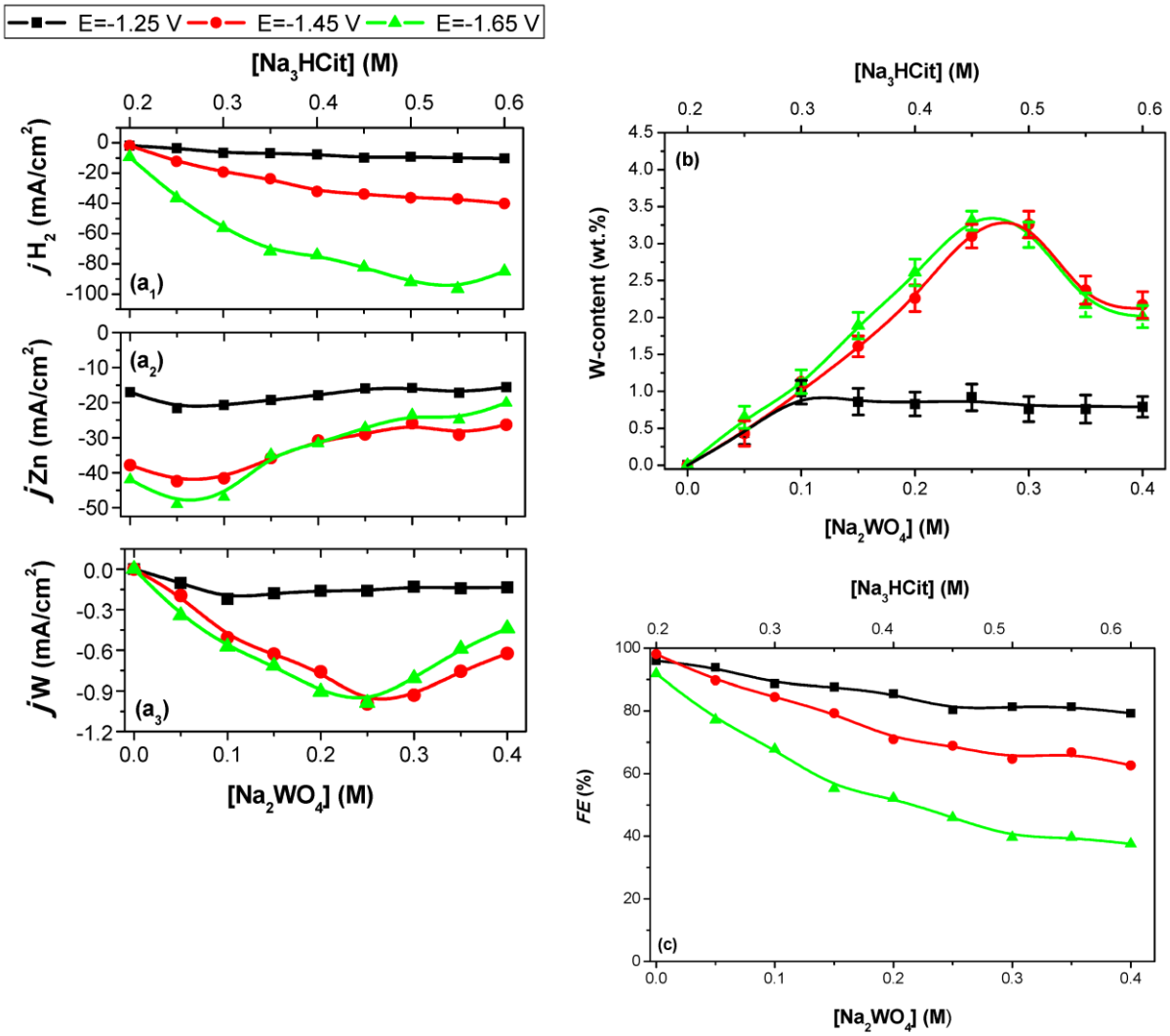

Figure 5. The effect of tungstate–citrate ion concentrations in the electrolyte on the electrodeposition process. The partial current densities of hydrogen (**a**$_1$), Zn (**a**$_2$) and W (**a**$_3$) in their codeposition. (**b**) The dependence of the W-content in the Zn–W deposits and (**c**) faradaic efficiency on the sodium tungstate and sodium citrate concentrations in the electrolyte, for three applied potentials (−1.25, −1.45, and −1.65 V vs. SCE), (0.20–0.60) M Na_3HCit, (0–0.40) M Na_2WO_4, 0.20 M $ZnSO_4$. pH = 5.7, ω = 1000 rpm, Q = 40 C/cm^2, T = 25 °C, Cu substrate.

In the case of Zn–W deposition at −1.25 V vs. SCE, the partial current of W co-discharge increased only slightly, when the Na_2WO_4 concentration in the plating bath was increased up to 0.10 M. Next, it remained at the same level with further increase in sodium tungstate concentration (Figure 5a$_2$). These trends are in accordance with the prediction of the thermodynamic model, according to which the $WO_4H_3Cit^{3-}$ complex fraction in the bath grows only up to ca. 0.10 M Na_2WO_4 in solution (Figure 6). This implies that, at low polarization (the area of the first local maximum in Figure 2a$_5$), W is codeposited with Zn only via the reduction of $WO_4H_3Cit^{3-}$.

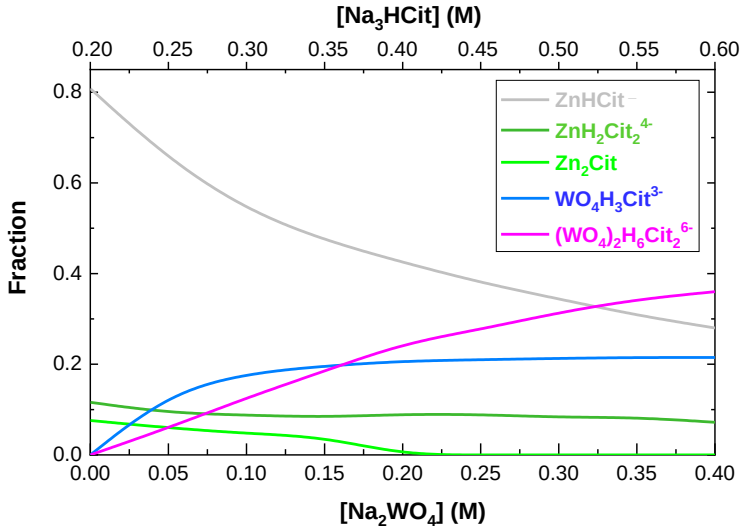

Figure 6. The distribution of species in the Zn–W–Cit system as a function of total dissolved sodium tungstate and sodium citrate concentration solution containing, for electrolytes containing (0.20–0.60) M Na_3HCit, (0–0.40) M Na_2WO_4, 0.20 M $ZnSO_4$, pH = 5.7.

The codeposition of Zn–W at higher polarization (−1.45 or −1.65 V vs. SCE) has two distinct regimes, depending on the ratio of W(VI)–Cit to Zn(II)–Cit species concentrations in the plating solution. The partial current of W codeposition at −1.45 and −1.65 V vs. SCE grows significantly with the increase in tungsten ion concentration up to 0.25 M (Figure 5a$_2$), in correspondence with the substantial increase in $(WO_4)_2H_4Cit_2^{6-}$ fraction in the electrolyte (Figure 6). This indicates the codeposition of both $WO_4H_3Cit^{3-}$ and $(WO_4)_2H_4Cit_2^{6-}$ at higher overpotentials (the area of the second local maximum in Figure 2a$_5$). The increase in $(WO_4)_2H_4Cit_2^{6-}$ species fraction correlates with a simultaneous decrease in $ZnHCit^-$ complex fraction in the electrolyte (Figure 6). The combination of both results in a substantial increase in W-content in the deposit, from ca. 0.5 wt.% at 0.05 M Na_2WO_4 to ca. 3.3 wt.% at 0.25 M Na_2WO_4 (Figure 5b). The decrease in the W partial current observed with a further increase in Na_2WO_4 concentration (Figure 5a$_3$) could be because the total fraction of the tungstate–citrate species increases beyond that of the total fraction of zinc–citrate complexes in the electrolyte (Figure 6). This indicates that W co-reduction is dependent on Zn deposition; significantly lower rates of Zn reduction (Figure 5a$_2$) result in a simultaneous decrease in the W reduction rate (Figure 5a$_3$).

Furthermore, the local maxima of Zn reduction become noticeable at ca. 0.05 M Na_2WO_4 and 0.25 M Na_3HCit, for all three applied potentials, indicating the possibility of the reduction of both $ZnHCit^-$ and Zn_2Cit^0 ions (Figure 6). When the Zn_2Cit^0 ions fraction approaches zero, with the increase in tungstate–citrate ion concentration, the trend of Zn partial current changes to a milder decrease, in correspondence with the milder decrease in $ZnHCit^-$ (Figure 5a$_3$). The increase in W content in the deposited Zn–W layers results in an increase in the hydrogen evolution rate due to a lower hydrogen overpotential on W compared to Zn [66], (Figure 5a$_1$), which in turn results in a decrease in faradaic efficiency of the deposition process, from ca. 95% for pure Zn deposition, to 64% for Zn–3.3W (wt.%) at −1.45 V vs. SCE, to 45% for Zn–3.3W at −1.65 V vs. SCE (Figure 5b,c).

3.6. Characterization of the Zn–W Deposits

Four elements were detected by XPS at the chosen samples: Zn, W, O, and C (Table 1). It should be noted that the Zn–W layers were exposed to air for several minutes right after the electrodeposition process, before placement in the XPS pre-chamber. Hence, it can be assumed that oxygen and carbon observed in high concentrations on the sample surfaces are associated with the high surface reactivity of freshly electrodeposited coatings, metal oxidation, and carbon adsorption from air. Carbon content drops from 33 to 52 at.% to

2%–5% (Table 1), indicating that it is a common carbon adsorption phenomenon [67]. In addition, some decrease in oxygen content within the deposited layer is observed, albeit to a significantly lesser extent (Table 1). This indicates the incorporation of some oxides into the Zn–W layers and their continuous distribution in the samples volume. One peak appears in the Zn 2p core level spectra at ca. 1021.8 eV; it can be assigned to the metallic Zn phase. The Zn peak becomes narrower and asymmetric after sputtering in all five analyzed samples. This indicates that a certain bond is preferentially removed from the surface; this may be related to an oxidized metal surface or oxy-carbon adsorbates. XPS analysis of the main W 4f peak reveals three main bonds (Figure 7, Table 2): W in Zn–W alloy, WO_2 and WO_3 at the surface of "as-deposited" samples as well as after sputter cleaning [68–70].

Table 1. XPS analysis of elemental atomic concentrations at the surfaces of Zn–W layers deposited from baths with different pH values at three different potentials, before (a_1–e_1) and after (a_2–e_2) 0.5 min Ar^+ ion sputtering.

Electrodeposition Conditions	Location	Zn (at.%)	W (at.%)	O (at.%)	C (at.%)
E = −1.25 V	a_1	14.81	0.31	36.26	48.62
pH = 3.0	a_2	84.18	0.95	13.06	1.82
E = −1.25 V	b_1	18.22	0.26	37.69	43.84
pH = 4.3	b_2	62.87	0.80	31.02	5.31
E = −1.25 V	c_1	21.01	0.90	37.88	40.21
pH = 5.7	c_2	69.48	1.41	26.60	2.50
E = −1.45 V	d_1	23.87	1.13	41.86	33.14
pH = 5.7	d_2	58.78	1.88	35.65	3.70
E = −1.65 V	e_1	13.42	1.19	33.40	51.99
pH = 5.7	e_2	68.47	2.23	27.39	1.94

Table 2. Parameters of the deconvolved W4f spectra for the Zn–W layers deposited from baths with different pH values at three different potentials, before (a_1–e_1) and after (a_2–e_2) 0.5 min Ar^+ ion sputtering.

Electrodeposition Conditions	Location	WO_3 (% Area)	WO_2 (% Area)	Zn–W Alloy (% Area)	Unknown Spectral Line (% Area)
E = −1.25 V	a_1	44.30	6.72	28.65	20.34
pH = 3.0	a_2	56.90	12.62	30.48	0.00
E = −1.25 V	b_1	76.73	16.53	6.74	0.00
pH = 4.3	b_2	95.75	0.00	4.25	0.00
E = −1.25 V	c_1	80.83	19.17	0.00	0.00
pH = 5.7	c_2	83.49	12.29	4.22	0.00
E = −1.45 V	d_1	67.96	32.04	0.00	0.00
pH = 5.7	d_2	86.00	12.12	1.88	0.00
E = −1.65 V	e_1	58.51	41.49	0.00	0.00
pH = 5.7	e_2	76.80	17.03	6.18	0.00

The tungsten metallic peak is shifted to lower binding energy, BE, compared with clean W due to alloying. When the sample that was electrodeposited at −1.25 V from a bath with pH = 3.0 (Figure 7a_1,a_2) was cleaned by ion sputtering for 1 min, the W metallic peak became the major peak, indicating that almost all of the oxide was removed and the substrate was exposed. Also, an unknown spectral line is observed in this sample only (Figure 7a_1) at a lower energy compared to the alloy peak; this peak is removed after sputtering (Figure 7a_2). Further investigation is required in order to understand the nature of this peak.

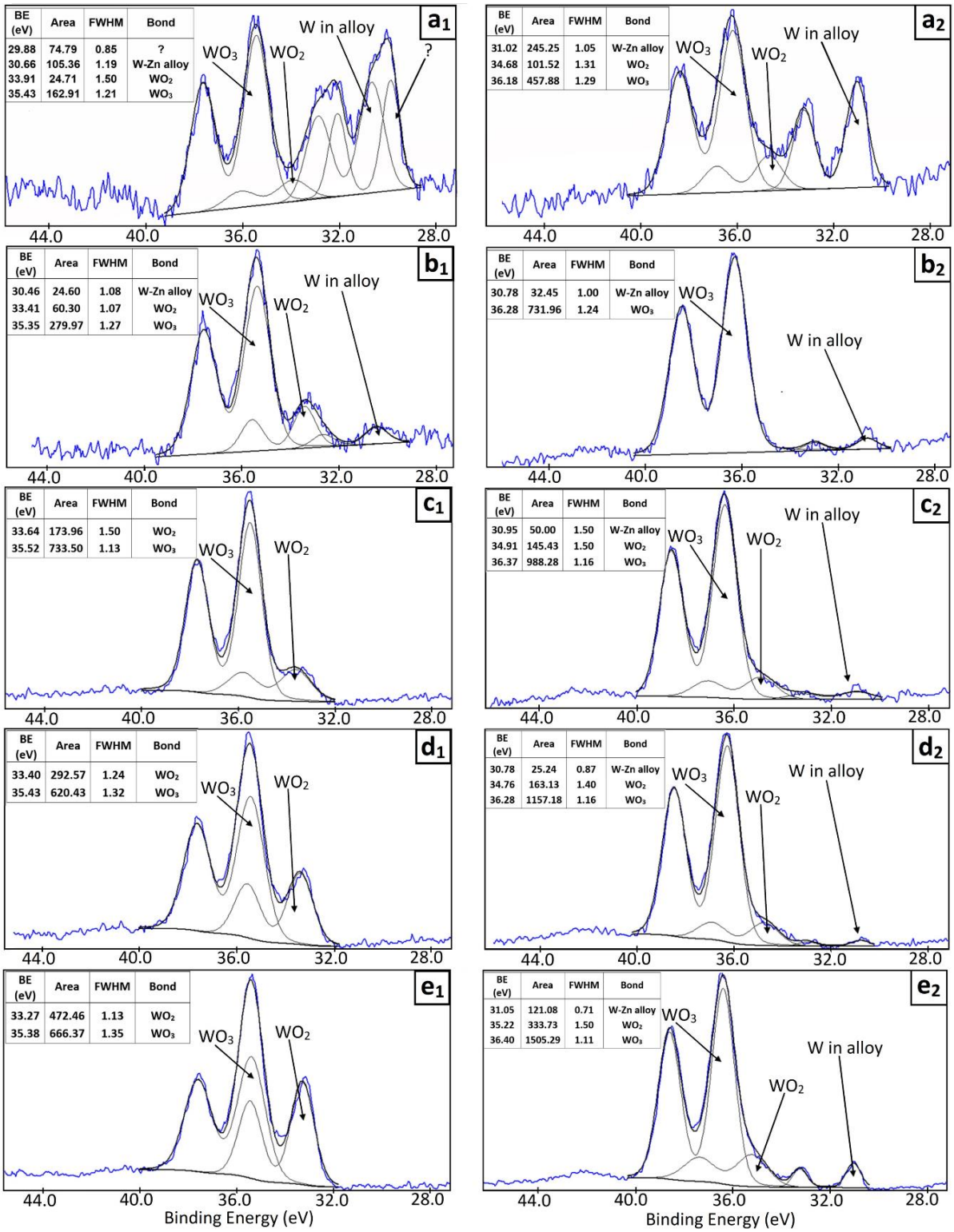

Figure 7. High-resolution XPS spectra of W4f core level with deconvolution on the component peaks obtained before (**a**$_1$–**e**$_1$) and after (**a**$_2$–**e**$_2$) ion sputtering. Zn–W layers deposited from baths with three different pH values and three deposition potentials. Electrolyte solution composition: 0.40 M Na_3HCit, 0.20 M $ZnSO_4$, 0.20 M Na_2WO_4. ω = 2000 rpm, Q = 20 C/cm^2, T = 25 °C, Cu substrate. (**a**$_1$,**a**$_2$) pH = 3.0, E = −1.25 V vs. SCE, (**b**$_1$,**b**$_2$) pH = 4.3, E = −1.25 V vs. SCE, (**c**$_1$,**c**$_2$) pH = 5.7, E = −1.25 V vs. SCE, (**d**$_1$,**d**$_2$) pH = 5.7, E = −1.45 V vs. SCE, (**e**$_1$,**e**$_2$) pH = 5.7, E = −1.65 V vs. SCE.

The W alloy peak is much more visible in the sample deposited from a bath with pH = 3.0 compared to other samples, both before (Figure 7a_1) and after (Figure 7a_2) sputter cleaning. W in the form of an alloy bond is visible only in the sample deposited at pH = 4.3 (Figure 7b_1), both before and after sputter cleaning. This may suggest that the oxide thickness is much lower in the samples deposited at pH = 3.0 (Figure 7a_1,a_2) and pH = 4.3 (Figure 7b_1,b_2) than in the samples deposited at pH = 5.7 (Figure 7c_1–e_2). However, since the samples were electrodeposited on the same day and were stored under the same conditions, this seems unlikely. Moreover, oxygen content on the surface of all five samples remained at a similar level (ca. 38 ± 4 at.%), while it differed significantly in deeper regions of the layer, depending on the deposition conditions (Table 1). This clearly indicates that different amounts of oxides are formed in the bulk of the layers as a result of different deposition conditions. The (W–Zn alloy)/(WO_3 + WO_2) ratio is the highest in the case of Zn–W alloy electrodeposited at pH = 3.0 (Figure 7a_1,a_2, Table 2), i.e., when the $WO_4H7Cit_2^{3-}$ complex is the dominant tungsten species being reduced on the cathode with ZnH_2Cit^0 species (Figure 1). For a bath pH of 4.3, the ratio of tungsten in an alloy to tungsten in oxides is ca. one order of magnitude lower than in the case of a bath with pH = 3.0 (Table 2). This corresponds to a decrease in $WO_4H_7Cit_2^{3-}$ ion concentration and the occurrence of another tungstate–citrate species, $WO_4H_4Cit^{2-}$, in the plating bath (Figure 1). In the case of Zn–W layers deposited from a bath with pH = 5.7, the dominant tungsten species in the plating bath are $WO_4H_3Cit^{3-}$ and the much more negative $(WO_4)_2H_6Cit_2^{6-}$ ion. XPS spectra of Zn–W layers deposited under such conditions show only a slightly visible peak of metallic tungsten, and only after sputter cleaning (Figure 7c_2,d_2,e_2). The (W–Zn alloy)/(WO_3 + WO_2) ratio is the same for layers deposited at –1.25 V from baths with either pH = 4.3 or pH = 5.7 (Figure 7b_2,c_2, Table 2). Under such conditions, only $WO_4H_7Cit_2^{3-}$ and $WO_4H_3Cit^{3-}$ complexes are reduced in baths with pH = 4.3 or pH = 5.7, respectively. Deposition at –1.45 V vs. SCE from a bath with pH = 5.7 results in a decrease in the amount of metallic tungsten codeposited with zinc compared to an alloy deposited at –1.25 V vs. SCE (Table 2), when both tungstate–citrate species, $WO_4H_3Cit^{3-}$ and $(WO_4)_2H_6Cit_2^{6-}$ are reduced (Figures 5 and 6). This indicates that at a deposition potential of –1.45 V vs. SCE, the hexavalent complex $(WO_4)_2H_6Cit_2^{6-}$ is mainly reduced to an oxide form on the cathode. Higher cathodic polarization (E = −1.65 V vs. SCE) leads to the increase in the (W–Zn alloy)/(WO_3 + WO_2) ratio by half compared to deposition at E = −1.25 V, and more than three times compared to deposition at E = −1.45 V vs. SCE (Table 2). This indicates that both the trivalent and hexavalent tungstate–citrate species present in the bath with pH = 5.7 can be reduced to the metal form at sufficiently high cathodic polarization (E = −1.65 V vs. SCE).

The surface morphology of Zn–W layers clearly depends on the electrodeposition potential (Figure 8). The coating deposited at –1.25 V exhibits a relatively integrated surface build of polygonal particles, similar for three bath pH values (Figure 8a_1,b_1,c_1). The surface of coatings deposited at higher cathodic potentials depends also on the pH of the plating bath. The surface of the Zn–W layer deposited at –1.45 V and –1.65 V vs. SCE and pH = 3.0 also consists of polygonal particles, which are much more developed compared to layers deposited at –1.25 V (Figure 8a_2,a_3). Layers deposited at –1.45 V from baths with pH = 4.3 or 5.7 exhibit a laterally uniform flake-like morphology, with noticeably more coarse grains in the case of a bath with pH = 4.3 (Figure 8b_2,c_2). Finally, the surface morphology of Zn–W coatings electrodeposited at –1.65 V is more nodular and fine-grained (Figure 8b_3,c_3). These changes in surface morphology could be related to variations in the chemical composition of the Zn–W layers deposited from different plating baths at various deposition potentials (Figure 8). Nevertheless, Figure 9 shows that the surface morphology of Zn–W deposits does not change considerably with the change in Zn–W layer composition but at the same applied potential and a constant bath pH. The increase in the W-content in Zn–W layers deposited at –1.25 V from a bath with pH = 3.0 was achieved by the modification of hydrodynamic conditions. Samples deposited under such conditions are made of relatively uniformly distributed, polygonal particles independently of the W-content codeposited

with Zn, which varies from ca. 0.75 to 1.90 wt.% W (Figure 9a_1–a_4). This finding is in line with the SEM observations in Figure 8a_1. The increase in W-content in layers deposited at –1.65 V from a bath with pH = 5.7 was achieved by the simultaneous increase in Na_2WO_4 and Na_2HCit concentrations in the electrolyte solution. Also, in this case, the effect of Zn–W layer composition (which varies from 0.50 to 3.5 wt.% W) on its surface morphology is insignificant (Figure 9b_1–b_4). All samples exhibit a similar nodular surface morphology, which is in line with the coating morphology obtained under similar conditions shown in Figure 8c_3.

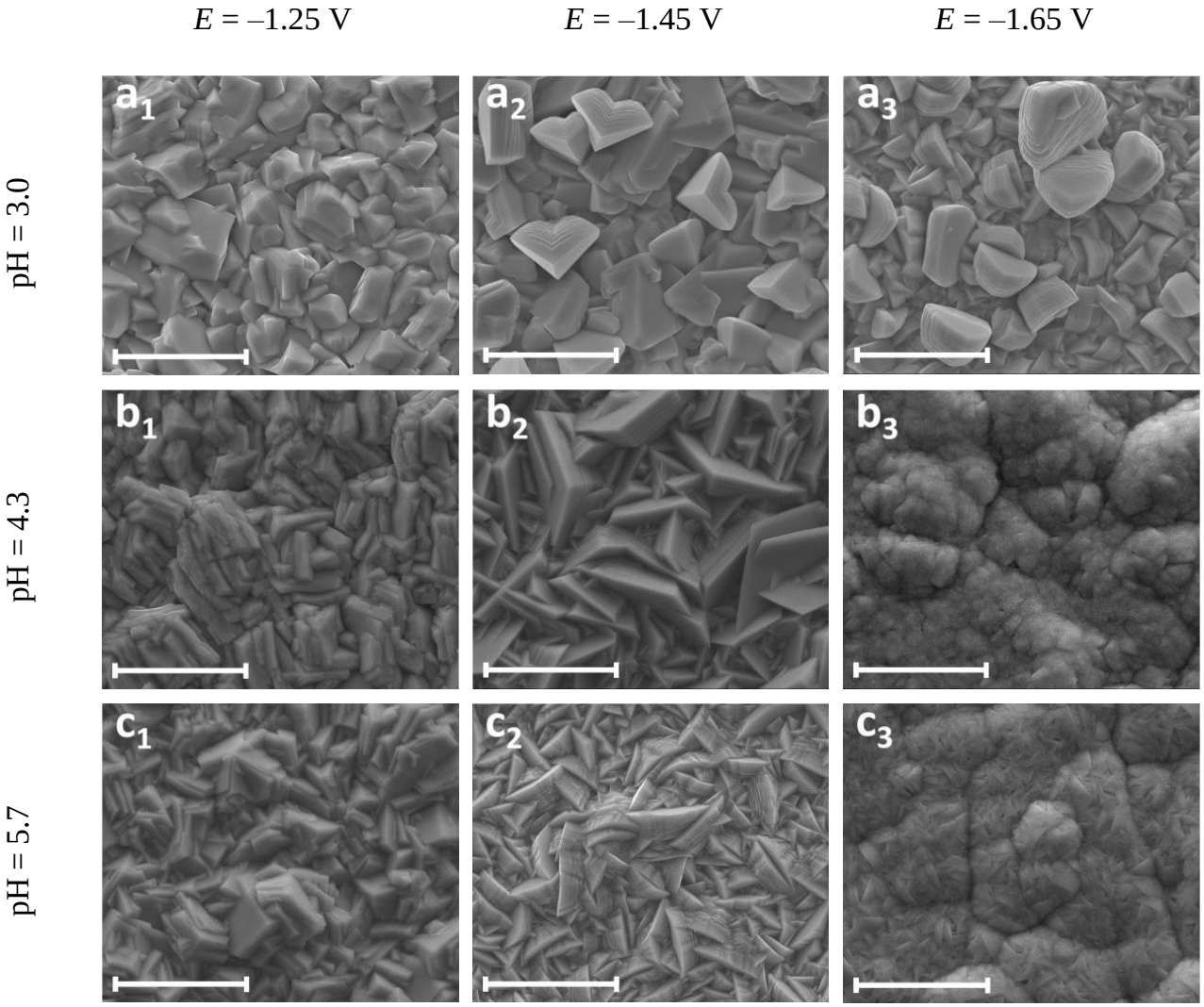

Figure 8. SEM secondary electrons (SE) images of Zn–W coatings with various W-contents, deposited at three applied potentials from electrolytes with three different pH values on a Cu substrate. Electrolyte solution composition: 0.30 M Na_3HCit, 0.20 M $ZnSO_4$, 0.10 M Na_2WO_4. ω = 250 rpm, Q = 20 C/cm^2, T = 25 °C. (**a_1**) 0.91 ± 0.14 wt.% W, (**a_2**) 0.38 ± 0.13 wt.% W, (**a_3**) 0.21 ± 0.13 wt.%, (**b_1**) 0.74 ± 0.17 wt.% W, (**b_2**) 0.60 ± 0.13 wt.% W, (**b_3**) 0.51 ± 0.14 wt.% W, (**c_1**) 0.83 ± 0.16 wt.% W, (**c_2**) 0.78 ± 0.12 wt.% W, (**c_3**) 1.1 wt.% ± 0.17 wt.% W. Scale bars equal 10 μm.

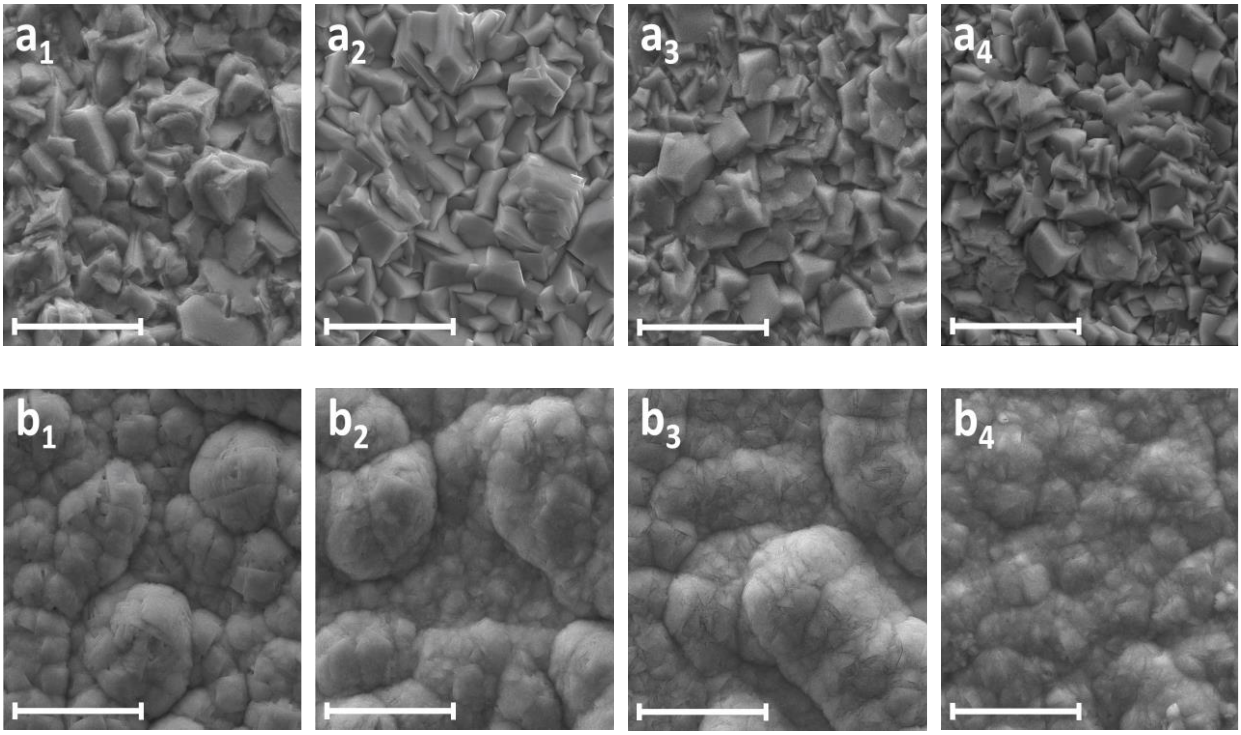

Figure 9. SEM SE images of Zn–W coatings with various W-contents, deposited at two different applied potentials from electrolytes with two different pH values on Cu substrate, T = 25 °C. Electrolyte solution composition: 0.30 M Na_3HCit, 0.20 M $ZnSO_4$, 0.10 M Na_2WO_4. Q = 20 C/cm^2, ω = 250–2000 rpm, E = −1.25 V vs. SCE (**a$_1$**–**a$_4$**); (0.20–0.60) M Na_3HCit, (0–0.40) M Na_2WO_4, 0.20 M $ZnSO_4$. pH = 5.7, ω = 1000 rpm, Q = 40 C/cm^2, E = −1.65 V vs. SCE (**b$_1$**–**b$_4$**); (**a$_1$**) 0.75 ± 0.18 wt.% W, (**a$_2$**) 1.0 ± 0.10 wt.% W, (**a$_3$**) 1.38 ± 0.10 wt.% W, (**a$_4$**) 1.86 ± 0.12 wt.% W, (**b$_1$**) 0.54 ± 0.15 wt.% W, (**b$_2$**) 1.90 ± 0.18 wt.% W, (**b$_3$**) 2.55 ± 0.16 wt.% W, (**b$_4$**) 3.45 ± 0.13 wt.% W. Scale bars equal 10 μm.

XRD characterization of Zn–W layers was carried out at room temperature immediately after deposition, for two sets of samples with varying tungsten contents (Figure 10). XRD did not detect the presence of either tungsten oxides or pure metallic W. Three phases appear in all XRD patterns: hexagonal Zn–W phase resulting from the substitution of Zn atoms by W atoms in the Zn crystal lattice, cubic Cu–Zn around the coating/Cu-substrate interface due to diffusion processes, and cubic Cu phase of the Cu substrate (Figure 10a). Substitutional W atoms cause changes in the unit cell parameters; lattice parameter c decreases while lattice parameter a increases when the W-content in the deposits increases (Figure 10b$_1$,c$_1$). The cause of these changes is the higher atomic radius of W compared to Zn (1.93 Å vs. 1.42 Å [71]) and the formation of a Zn–W hexagonal phase. This characteristic change in lattice parameters is much more significant in the case of Zn–W layers deposited at –1.25 V vs. SCE from a bath with pH = 3.0 (Figure 10b$_1$) compared to layers deposited at –1.65 V vs. SCE from a bath with pH = 5.7 (Figure 10c$_1$). This finding is in line with the XPS results showing that the Zn–W layers formed in a bath with pH = 3.0 contain a much higher amount of tungsten in metallic form (Figure 7a$_1$,a$_2$) than the other Zn–W layers, including those deposited from a bath with pH = 5.7 (Figure 7b$_1$–e$_2$). Furthermore, a decrease in the Zn–W crystallite size is observed with the increase in the W-content (Figure 10b$_2$,c$_2$). This is considered advantageous for corrosion resistance, due to a higher grain boundary density on the surface of fine-grained coatings in comparison with coarse-grained layers [72].

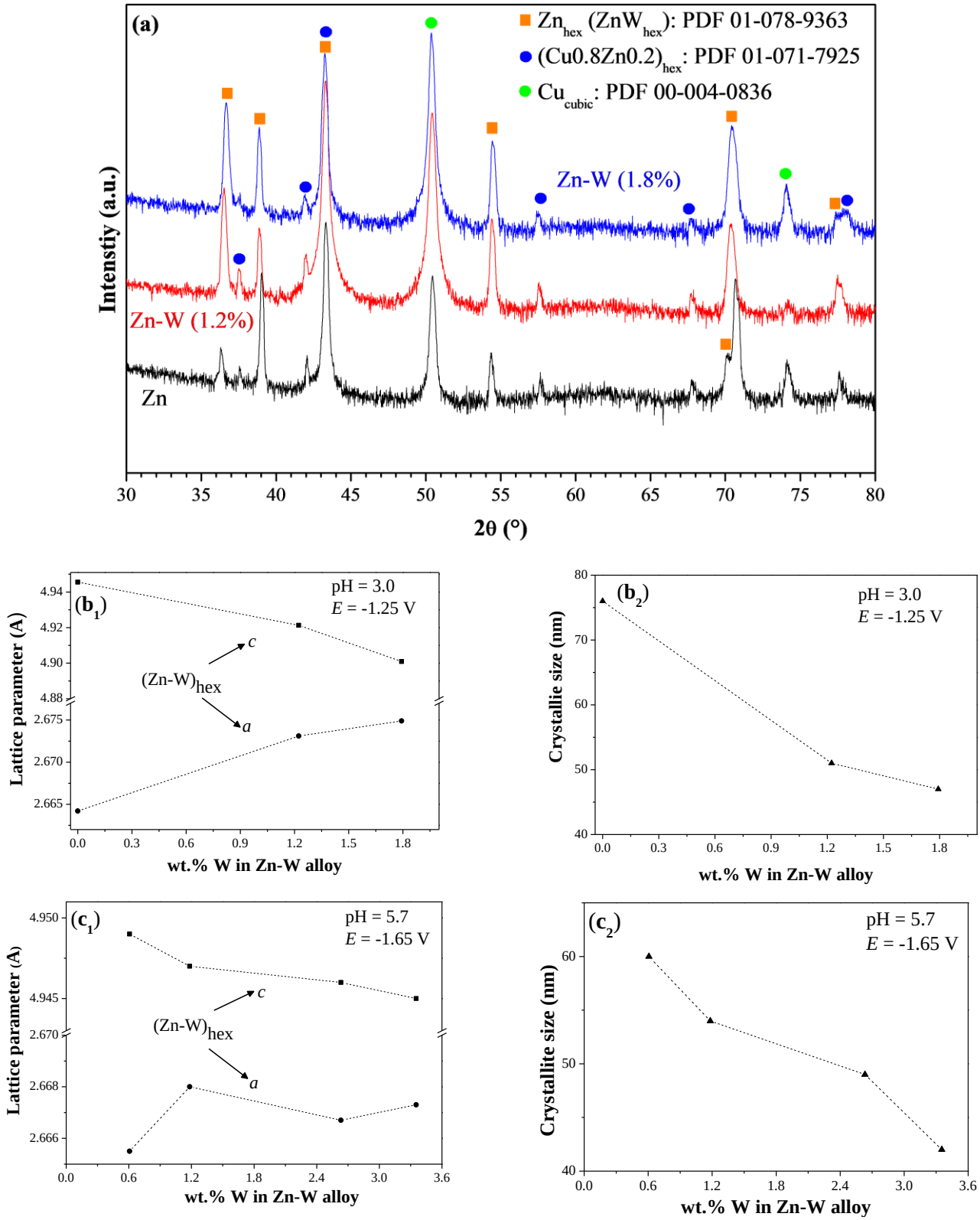

Figure 10. (**a**) XRD patterns from different coatings with up to 1.8 wt.% W. (**b$_1$**,**c$_1$**) Dependence of the values of the unit cell parameters of the ZnW phase on the content of W. (**b$_2$**,**c$_2$**) Dependence of the crystallite size on the content of W. (**b$_1$**,**b$_2$**) Zn–W deposits obtained from a bath with pH = 3.0 at $E = -1.25$ V. (**c$_1$**,**c$_2$**) Zn–W deposits obtained from a bath with pH = 5.7 at $E = -1.65$ V.

3.7. The Mechanism of Zn–W Codeposition

Reactions (1)–(9) list the reduction reactions that may take place in the Zn(II)–W(VI)–Cit system:

$$ZnH_2Cit^0 + 2e^- \rightarrow Zn^0 + H_2Cit^{2-} \quad (1)$$

$$ZnHCit^- + H_2O + 2e^- \rightarrow Zn^0 + H_2Cit^{2-} + OH^- \quad (2)$$

$$Zn_2Cit^0 + 2H_2O + 4e^- \rightarrow 2Zn^0 + H_2Cit^{2-} + 2OH^- \quad (3)$$

$$WO_4H_7Cit_2{}^{3-} + H_2O + 6e^- \rightarrow W^0 + 2H_2Cit^{2-} + 5OH^- \quad (4)$$

$$WO_4H_4Cit^{2-} + 2H_2O + 6e^- \rightarrow W^0 + H_2Cit^{2-} + 6OH^- \quad (5)$$

$$WO_4H_3Cit^{3-} + 3H_2O + 6e^- \rightarrow W^0 + H_2Cit^{2-} + 7OH^- \quad (6)$$

$$(WO_4)_2H_6Cit_2{}^{6-} + 6H_2O + 12e^- \rightarrow 2W^0 + 2H_2Cit^{2-} + 14OH^- \quad (7)$$

$$H_3Cit^- + 2e^- \rightarrow H_2 + HCit^{3-} \quad (8)$$

$$2H_2Cit^{2-} + 2e^- \rightarrow H_2 + 2HCit^{3-} \quad (9)$$

At pH = 3.0, Zn–W codeposition occurs through the reduction of ZnH_2Cit^0 and $WO_4H_7Cit_2{}^{3-}$ ions (Reactions (1) and (4), respectively). W deposition from $WO_4H_7Cit_2{}^{3-}$ shows a maximal rate at potential of ca. –1.30 V vs. SCE (Figure 2a$_3$). Zn–W deposition at pH = 3.0 is accompanied by a relatively high rate of hydrogen evolution (Figure 2a$_1$, Reactions (8) and (9)). This happens via deprotonation of the carboxyl groups of the H_3Cit^- ions (Reaction (8), Figure 1) and H_2Cit^{2-} ions (Reaction (9)) that are a by-product of the Zn and W deposition (Reactions (1) and (4)). The hydroxyl group in the $HCit^3$ ion, which is formed in Reactions (8) and (9), is not considered as a potential proton donor here, because it is known that the hydroxyl group deprotonates only at highly alkaline pH values, estimated to be between 11 and 14.4 [56,73].

Zn deposition through the reduction of three different Zn(II)–Cit species may occur in a bath with pH = 4.3 (Reactions (1) through (3)). ZnH_2Cit^0 and Zn_2Cit^0 complexes are known to be able to form polymers in which the ligand neutralizes the metal charge by binding to the metal simultaneously through various groups, and the resultant polymers form insoluble solid phases. However, such a process needs long time to occur [59]; by then, the abovementioned complexes, which are electroactive, can be reduced on the cathode. However, the amount of Zn_2Cit^0 in solution is very low at pH = 4.3; hence, Reaction (3) is negligible. W can be deposited at pH = 4.3 via the reduction of $WO_4H_7Cit_2{}^{3-}$ and $WO_4H_4Cit^{2-}$ ions (Reactions (4) and (5)).

In a bath with pH = 5.7, Zn deposition occurs mainly via the reduction of $ZnHCit^-$ ions (Reaction (2)); yet, Reaction (3), of Zn_2Cit^0, is also possible. W deposition via only $WO_4H_3Cit^{3-}$ (Reaction (6)) takes place at lower polarization (ca. $E = -1.25$ V vs. SCE). Shifting the deposition potential towards more negative values results in the reduction of two W(VI)–Cit species: $WO_4H_3Cit^{3-}$ and $(WO_4)_2H_6Cit_2{}^{6-}$ (Reactions (6) and (7)).

It should be emphasized that not all the tungsten codeposited with zinc from the aqueous citrate solution is in metallic form, and that the ratio of Zn–W alloy to tungsten oxides depends on the bath pH and deposition potential (Figure 7). This indicates that the tungsten deposition processes described herein by Reactions (4)–(7) are in reality much more complex, involving multiple steps which sometimes lead only to a partial reduction of W(VI)–Cit species and codeposition of tungsten oxides with metallic Zn.

Different kinetic regimes of Zn and W codeposition observed for deposition from a bath with pH = 3.0 (Figure 3a$_2$,a$_3$) implies that the W(VI) and Zn(II) complex ions are transported to and discharged on the cathode separately. Hence, a theory introduced by

Younes and Gileadi [74], according to which the intermediate mixed-metal complex serves as a precursor for tungsten alloy codeposition, can be excluded herein. On the other hand, the results obtained for the deposition from baths pH = 4.3 (Figure 3b_2,b_3) and pH = 5.7 (Figure 3c_2,c_3) reveal a correlation between the kinetic regimes of Zn and W deposition, suggesting that the formation of some intermediate Zn(II)–W(VI)–Cit complex and its transport and discharge on the cathode in the form of Zn–W is theoretically possible.

An earlier theory of Clark and Lietzke [39] postulated that the partly reduced tungstate film is first deposited on the cathode and is then catalytically reduced by hydrogen in the presence of freshly codeposited alloying metals (in that case, Fe, Co, and Ni). More recently, Oue et al. [75] described the Ni–W alloy deposition behavior by a mechanism of the electrochemical reduction of W(IV) intermediate oxide to W by atomic hydrogen adsorbed on the freshly deposited Ni, using its unpaired 3*d* electrons.

Our results, showing that the highest content of metallic W is codeposited with Zn from a bath with pH = 3.0 (Figure 7, Table 2) where the hydrogen evolution rate is the highest (Figure 2a_1) is in line with these hypotheses, showing a correlation between tungsten deposition and hydrogen evolution. However, the higher content of metallic W codeposited with Zn from a bath with pH = 3.0 compared to baths with pH = 4.3 or 5.7 can also be associated with different electrochemical properties of several dominant W(VI)–Cit and Zn(II)–Cit species, which are present in the bath at different pH values (Figure 1).

Induced codeposition of tungsten alloys is considered similar to induced codeposition of molybdenum alloys; hence, some analogies in their mechanisms can be discussed [33]. Chassaing et al. [76] suggested that intermediate molybdenum oxide, which is formed by molybdate reduction, transforms in the presence of Ni^{2+} ions into a mixed Ni–Mo oxide, which is further reduced by hydrogen to a Ni–Mo alloy at sufficiently high polarization. At low polarization, only a mixed oxide is deposited. Next, Gomez et al. [77] showed that, in the first step in induced codeposition of Co–Mo alloy, Mo(VI) ions are partially reduced to a Mo(IV) oxide. When low potential is applied, a continuous molybdenum oxide film is formed on the electrode, and Co–Mo is not deposited. More negative potentials are needed to induce the Co–Mo alloy deposition over an initial molybdenum oxide. However, in contrary to [75,76], no relation between Mo reduction and hydrogen reduction was shown by Gomez et al. [77]. It was only noted that a greater hydrogen evolution accompanies alloy deposition as a result of the threshold potential shift.

The example of Zn–W codeposition from a bath with pH = 5.7 at either –1.45 V or –1.65 V vs. SCE is in line with the abovementioned theories (see Figures 5 and 7d_2,e_2 and Table 2). The ratio of W–Zn alloy to tungsten oxides in the deposited coatings is 0.019 and 0.066 for deposition at –1.45 V and –1.65 V vs. SCE, respectively (Table 2). As described in Section 3.5, the same two W(VI)–Cit species, $WO_4H_3Cit^{3-}$ and $(WO_4)_2H_6Cit_2^{6-}$, are reduced on the cathode at both potentials (Figures 1, 5 and 6). The values of the partial current of tungsten reduction are of the same magnitude, so is the content of W in Zn–W deposit for both $E = -1.45$ V and –1.65 V (Figure 5a_3,b); it is only the ratio between different oxidation states of deposited tungsten that varies (Figure 7d_2,e_2). This indicates that the reduction of W(VI)–Cit ions to metallic W involves a step of formation of intermediate tungsten oxide, which is reduced to metallic tungsten at sufficiently high cathodic polarization, while, at a potential lower than threshold values—tungsten oxides are formed.

The higher amount of metallic W codeposited with Zn at –1.65 V vs. SCE is clearly related to the much higher hydrogen evolution rate, compared to the process at –1.45 V (Figure 5). However, it cannot be unequivocally determined at this stage if the hydrogen evolution affects the metallic tungsten codeposition, or if it just accompanies the Zn–W deposition process with the higher rate simply due to higher polarization.

4. Conclusions

Metallic W can be electrodeposited with Zn from aqueous citrate solutions. Zn–W alloy layers were successfully electrodeposited on Cu substrates from aqueous citrate baths with pH ranging from 3.0 to 5.7, at faradaic efficiency as high as 90%. The W-content in the

Zn–W deposit is closely related to the concentration of the electroactive tungstate–citrate species and to the zinc–citrate electroactive species in the electrolyte solution. Hence, the composition of the coatings can be controlled by variations in the tungstate and citrate ion concentrations in the bath. The maximal concentration of W in the Zn–W layers deposited in this work was 3.5 wt.%. The oxidation state of tungsten in the Zn–W layers can be controlled by adjustment of the bath pH and applied potential. The surface morphology of the Zn–W coatings does not depend on the W-content in the deposit; it does depend, however, on the applied potential and bath pH. The deposited Zn–W layers are compact, uniform macroscopically, and crack-free microscopically. A hexagonal Zn–W phase is formed, with W atoms substituting Zn atoms in the Zn crystal lattice. An increase in the W-content in the Zn–W alloy results in a decrease in the crystallite size of the hexagonal Zn–W phase. The formation of stable and electroactive W(VI) and Zn(II) complexes is the first indispensable factor enabling Zn–W-induced codeposition. Further research is necessary to fully understand this multi-step induced codeposition of Zn–W from citrate-based aqueous solutions.

Supplementary Materials: The following supporting information can be downloaded at https://www.mdpi.com/article/10.3390/coatings13122001/s1. Figure S1: Cross section of Zn–W (1.21 ± 0.11 wt.% W) coating electrodeposited on Cu (a) and EDS maps of elemental distribution within the sample (b–d). Electrolyte solution composition: 0.32 M Na_3HCit, 0.20 M $ZnSO_4$, 0.12 M Na_2WO_4, pH = 3.0, $E = -1.25$ V vs. SCE, Q = 40 C/cm^2, ω = 1000 rpm. Scale bars equal 10 μm. Figure S2: Cross section of Zn–W (3.51 ± 0.22 wt.% W) coating electrodeposited on Cu (a) and EDS maps of elemental distribution within the sample (b–d). Electrolyte solution composition: 0.40 M Na_3HCit, 0.20 M $ZnSO_4$, 0.20 M Na_2WO_4, pH = 5.7, $E = -1.65$ V vs. SCE, Q = 40 C/cm^2, ω = 2500 rpm. Scale bars equal 10 μm.

Author Contributions: H.K.: conceptualization, data curation, investigation, methodology, visualization, writing—original draft. N.E.: conceptualization, funding acquisition, methodology, project administration, resources, supervision, visualization, writing—review and editing. All authors have read and agreed to the published version of the manuscript.

Funding: This research received no external funding.

Institutional Review Board Statement: Not applicable.

Informed Consent Statement: Not applicable.

Data Availability Statement: Data are contained within the article and supplementary materials.

Acknowledgments: We thank Davide Levi and Pini Shekhter from the Wolfson Applied Materials Research Center for their XRD and XPS tests and analyses, respectively.

Conflicts of Interest: The authors declare no conflict of interest.

References

1. McCain, W.C.; Crouse, L.C.B.; Bazar, M.A.; Roszell, L.E.; Leach, G.J.; Middleton, J.R.; Reddy, G. Subchronic oral toxicity of sodium tungstate in Sprague-Dawley rats. *Int. J. Toxicol.* **2015**, *34*, 336–345. [CrossRef]
2. Walker, D.E.; Wilcox, G.D. Molybdate based conversion coatings for zinc and zinc alloy surfaces: A review. *Trans. Inst. Met. Finish.* **2008**, *86*, 251–259. [CrossRef]
3. Keith, S.; Moffett, D.B.; Rosemond, Z.A.; Wohlers, D.W.; Amata, R.J.; Diamond, G.L.; Swarts, S.G. *Toxicological Profile for Tungsten*; Agency for Toxic Substances and Disease Registry: Atlanta, GA, USA, 2005.
4. Rashmi, S.; Elias, L.; Hegde, A.C. Multilayered Zn-Ni alloy coatings for better corrosion protection of mild steel. *Eng. Sci. Technol. Int. J.* **2017**, *20*, 1227–1232. [CrossRef]
5. Azizi, F.; Kahoul, A. Electrodeposition and corrosion behaviour of Zn/Co coating produced from a sulphate bath. *Trans. Inst. Met. Finish.* **2016**, *94*, 43–48. [CrossRef]
6. U.S. Department of Health and Human Services. *Report on Carcinogens*, 14th ed.; U.S. Department of Health and Human Services: Triangle Park, NC, USA, 2016.
7. Eichinger, E.; Osborne, J.; Van Cleave, T. Hexavalent chromium elimination: An aerospace industry progress report. *Met. Finish.* **1997**, *95*, 36–41. [CrossRef]
8. Brenner, A. *Electrodeposition of Alloys: Principles and Practice*; Academic Press: New York, NY, USA, 1963; Volume II.

9. Eliaz, N.; Gileadi, E. *Physical Electrochemistry: Fundamentals, Techniques, and Applications*, 2nd ed.; Wiley-VCH: Weinheim, Germany, 2019.
10. Koster, W.; Schmid, H. Über die Legierungsfähigkeit von Zink mit Wolfram und Molybdän. *Z. Metallkd.* **1955**, *46*, 462–463. [CrossRef]
11. Hodge, W.; Evans, R.M.; Haskins, A.F. Metallic Materials Resistant to Molten Zinc. *JOM* **1955**, *7*, 824–831. [CrossRef]
12. Kurtz, W.; Koch, E. Gmelin handbook of inorganic chemistry. In *Metal, Chemical Reactions with Metals Zinc to Lawrencium*; Springer: Berlin/Heidelberg, Germany, 1988.
13. Martinz, H.; Nigg, B.; Hoffmann, A. The corrosion behaviour of refractory metals against molten and evaporated zinc. In Proceedings of the 17th Plansee Seminar, Reutte, Austria, 25–29 May 2009.
14. Shabalin, I.L. *Ultra-High Temperature Materials I: Carbon (Graphene/Graphite) and Refractory Metals*; Springer: Dordrecht, The Netherlands, 2014.
15. Massalski, T.B.; Okamoto, H.; Subramanian, P.R.; Kacprzak, L. *Binary Alloy Phase Diagrams*, 2nd ed.; ASM International: Metals Park, OH, USA, 1990.
16. Cavallotti, P.L.; Nobili, L.; Vicenzo, A. Phase structure of electrodeposited alloys. *Electrochim. Acta* **2005**, *50*, 4557–4565. [CrossRef]
17. Sridhar, T.M.; Eliaz, N.; Gileadi, E. Electroplating of Ni4W. *ECS Solid-State Lett.* **2005**, *8*, C58–C61. [CrossRef]
18. Hegde, A.C.; Venkatakrishna, K.; Eliaz, N. Electrodeposition of Zn–Ni, Zn–Fe and Zn–Ni–Fe alloys. *Surf. Coat. Technol.* **2010**, *205*, 2031–2041. [CrossRef]
19. Sagiv, M.C.; Eliaz, N.; Gileadi, E. Incorporation of iridium into electrodeposited rhenium–nickel alloys. *Electrochim. Acta* **2013**, *88*, 240–250. [CrossRef]
20. Baik, S.I.; Duhin, A.; Phillips, P.J.; Klie, R.F.; Gileadi, E.; Seidman, D.N.; Eliaz, N. Atomic-scale structural and chemical study of columnar and multilayer Re–Ni electrodeposited thermal barrier coating. *Adv. Eng. Mater.* **2016**, *18*, 1133–1144. [CrossRef]
21. Eliaz, N.; Gileadi, E. Induced codeposition of alloys of tungsten, molybdenum and rhenium with transition metals. In *Modern Aspects of Electrochemistry*; Vayenas, C.G., White, R.E., Gamboa-Aldeco, M.E., Eds.; Springer: New York, NY, USA, 2008; Volume 42, Chapter 4; pp. 191–301.
22. Eliaz, N.; Sridhar, T.M.; Gileadi, E. Synthesis and characterization of nickel tungsten alloys by electrodeposition. *Electrochim. Acta* **2005**, *50*, 2893–2904. [CrossRef]
23. Gileadi, E.; Eliaz, N. The mechanism of induced codeposition of Ni-W alloys. *ECS Trans.* **2007**, *2*, 337–349. [CrossRef]
24. Fink, C.G.; Jones, F.L. The electrodeposition of tungsten from aqueous solutions. *Trans. Electrochem. Soc.* **1931**, *59*, 461–481. [CrossRef]
25. Holt, M.L. The co-deposition of tungsten and iron from aqueous solutions. *Trans. Electrochem. Soc.* **1934**, *66*, 453–460. [CrossRef]
26. Holt, M.L. Metals codeposited with tungsten from the alkaline tungsten plating bath. *Trans. Electrochem. Soc.* **1937**, *71*, 301–311. [CrossRef]
27. Holt, M.L.; Nielsen, M.L. Electrodeposition of iron-tungsten alloys from an acid plating bath. *Trans. Electrochem. Soc.* **1942**, *82*, 193–203. [CrossRef]
28. Brenner, A.; Burkhead, P.; Seegmiller, E. Electrodeposition of tungsten alloys containing iron, nickel, and cobalt. *J. Res. Natl. Bur. Stand.* **1947**, *39*, 351–383. [CrossRef]
29. Lietzke, M.H.; Holt, M.L. Codeposition of tungsten and iron from an aqueous ammoniacal citrate bath. *J. Electrochem. Soc.* **1948**, *94*, 252–261. [CrossRef]
30. Holt, M.L.; Vaaler, L.E. Electrolytic reduction of aqueous tungstate solutions. *J. Electrochem. Soc.* **1948**, *94*, 50–58. [CrossRef]
31. Akiyama, T.; Fukushima, H. Recent study on the mechanism of the electrodeposition of iron-group metal alloys. *ISIJ Int.* **1992**, *32*, 787–798. [CrossRef]
32. Silkin, S.A.; Gotelyak, A.V.; Tsyntsaru, N.I.; Dikusar, A.I. Electrodeposition of alloys of the iron group metals with tungsten from citrate and gluconate solutions: Size effect of microhardness. *Surf. Eng. Appl. Electrochem.* **2017**, *53*, 7–14. [CrossRef]
33. Tsyntsaru, N.; Cesiulis, H.; Donten, M.; Sort, J.; Pellicer, E.; Podlaha-Murphy, E.J. Modern trends in tungsten alloys electrodeposition with iron group metals. *Surf. Eng. Appl. Electrochem.* **2012**, *48*, 491–520. [CrossRef]
34. Vernickaite, E.; Tsyntsaru, N.; Cesiulis, H. Electrodeposited Co-W alloys and their prospects as effective anode for methanol oxidation in acidic media. *Surf. Coat. Technol.* **2016**, *307*, 1322–1328. [CrossRef]
35. Yar-Mukhamedova, G.; Ved, M.; Sakhnenko, N.; Nenastina, T. Electrodeposition and properties of binary and ternary cobalt alloys with molybdenum and tungsten. *Appl. Surf. Sci.* **2018**, *445*, 298–307. [CrossRef]
36. Vernickaite, E.; Tsyntsaru, N.; Sobczak, K.; Cesiulis, H. Electrodeposited tungsten-rich Ni-W, Co-W and Fe-W cathodes for efficient hydrogen evolution in alkaline medium. *Electrochim. Acta* **2019**, *318*, 597–606. [CrossRef]
37. El Boraei, N.F.; Ibrahim, M.A.M. Preparation, characterisation and electrochemical study of crack-free nanocrystalline electrodeposited Co-W alloy coating of high hardness. *Trans. Inst. Met. Finish.* **2020**, *98*, 234–242. [CrossRef]
38. Rogers, D.G.; Burr, A.A. Electrodeposition of chromium-tungsten alloy plates. *J. Electrochem. Soc.* **1950**, *97*, 67–69. [CrossRef]
39. Clark, W.E.; Lietzke, M.H. The mechanism of the tungsten alloy plating process. *J. Electrochem. Soc.* **1952**, *99*, 245–249. [CrossRef]
40. Bacal, P.; Indyka, P.; Stojek, Z.; Donten, M. Unusual example of induced codeposition of tungsten. Galvanic formation of Cu-W alloy. *Electrochem. Commun.* **2015**, *54*, 28–31. [CrossRef]
41. Bacal, P.; Stojek, Z.; Donten, M. Optimization of CuW alloy electrodeposition towards high-tungsten content. *J. Solid State Electrochem.* **2016**, *20*, 3143–3150. [CrossRef]

42. Vernickaite, E.; Tsyntsaru, N.; Cesiulis, H. Electrochemical co-deposition of tungsten with cobalt and copper: Peculiarities of binary and ternary alloys coatings formation. *Surf. Coat. Technol.* **2016**, *307*, 1341–1349. [CrossRef]
43. Saitou, M. Cu–W thin film electrodeposited in an aqueous solution. *Int. J. Electrochem. Sci.* **2017**, *12*, 4714–4723. [CrossRef]
44. Nakano, H.; Oue, S.; Taniguchi, S.; Kobayashi, S.; Fukushima, H. Effect of a small amount of Mo, W and Sn additives on the morphology and orientation of electrodeposited Zn. *Tetsu-To-Hagane/J. Iron Steel Inst. Japan* **2007**, *93*, 763–768. [CrossRef]
45. Sadjadi, S.A.S.; Bohlooli, F.; Zare-Dorabei, R. Electroless deposition of novel ternary Zn-W-B alloy coating. *Anal. Bioanal. Electrochem.* **2015**, *7*, 118–128.
46. Kazimierczak, H.; Ozga, P. Electrodeposition of Sn-Zn and Sn-Zn-Mo layers from citrate solutions. *Surf. Sci.* **2013**, *607*, 33–38. [CrossRef]
47. Kazimierczak, H.; Ozga, P.; Socha, R.P. Investigation of electrochemical co-deposition of zinc and molybdenum from citrate solutions. *Electrochim. Acta* **2013**, *104*, 378–390. [CrossRef]
48. Kazimierczak, H.; Hara, A.; Bigos, A.; Ozga, P. Electrodeposition of Zn-Mn-Mo layers from citrate-based aqueous electrolytes. *Electrochim. Acta* **2016**, *202*, 110–121. [CrossRef]
49. Gómez, E.; Pellicer, E.; Duch, M.; Esteve, J.; Vallés, E. Molybdenum alloy electrodeposits for magnetic actuation. *Electrochim. Acta* **2006**, *51*, 3214–3222. [CrossRef]
50. Kazimierczak, H.; Ozga, P.; Świa, Z.; Bielańska, E. Characterisation of Zn-Mo alloy layers electrodeposited from aqueous citrate solution. *J. Alloys Compd.* **2013**, *578*, 82–89. [CrossRef]
51. Kazimierczak, H.; Ozga, P.; Berent, K.; Kot, M. Microstructure and micromechanical properties of electrodeposited Zn-Mo coatings on steel. *J. Alloys Compd.* **2015**, *636*, 156–164. [CrossRef]
52. Kazimierczak, H.; Morgiel, J.; Swiatek, Z.; Vega, J.M.; García-Lecina, E. Effect of Mo addition on corrosion of Zn coatings electrodeposited on steel. *Corros. Sci.* **2018**, *135*, 107–119. [CrossRef]
53. Cervilla, A.; Ramirez, J.A.; Llopis, E. Compounds of tungsten(VI) with citric acid: A spectrophotometric; polarimetric; hydrogen-1, carbon-13 N.M.R. study of the formation and interconversion equilibria in aqueous solution. *Transit. Met. Chem.* **1986**, *11*, 186–192. [CrossRef]
54. Cruywagen, J.J.; Saayman, L.J.; Niven, M.L. Complexation between tungsten(VI) and citrate: The crystal and molecular structure of a dinuclear complex, $Na_6[W_2O_5(cit)_2]\cdot 10H_2O$. *J. Crystallogr. Spectrosc. Res.* **1992**, *22*, 737–740. [CrossRef]
55. Kazimierczak, H.; Ozga, P.; Jałowiec, A.; Kowalik, R. Tin-zinc alloy electrodeposition from aqueous citrate baths. *Surf. Coat. Technol.* **2014**, *240*, 311–319. [CrossRef]
56. Kazimierczak, H.; Szymkiewicz, K.; Rogal, Ł.; Gileadi, E.; Eliaz, N. Direct current electrodeposition of Zn-SiC nanocomposite coatings from citrate bath. *J. Electrochem. Soc.* **2018**, *165*, D526–D535. [CrossRef]
57. Pettit, L.D.; Powell, K.J. *The IUPAC Stability Constants Database, SC-Database for Windows*; Academic Software: Yorks, UK, 2012; Release 5.
58. Smith, W.R.; Missen, R.W. *Chemical Reactions Equilibrium Analysis: Theory and Algorithms*; John Wiley & Sons: Toronto, Canada, 1982.
59. Ozga, P. The thermodynamic models of complex electrolytic baths for electrodepostion of zinc and tin alloys. In *Polska Metalurgia w Latach 2006–2010*; Akapit: Krakow, Poland, 2010. (In Polish)
60. Puigdomenech, I. *MEDUSA (Make Equilibrium Diagrams Using Sophisticated Algorithms) Program, Ver. 26*; Royal Institute of Technology: Stockholm, Sweden, 2009.
61. Hamada, Y.Z.; Bayakly, N.; George, D.; Greer, T. Speciation of molybdenum(VI)-citric acid complexes in aqueous solutions. *Synth. React. Inorg. Met. Nano-Met. Chem.* **2008**, *38*, 664–668. [CrossRef]
62. Heller, A.; Barkleit, A.; Foerstendorf, H.; Tsushima, S.; Heim, K.; Bernhard, G. Curium(III) citrate speciation in biological systems: A europium(III) assisted spectroscopic and quantum chemical study. *Dalt. Trans.* **2012**, *41*, 13969–13983. [CrossRef]
63. Kazimierczak, H. *Electrodeposition of Zn-Mo Layers from Aqueous Citrate Solutions*; Institute of Metallurgy and Materials Science PAS: Kraków, Poland, 2014.
64. Hreid, T.; Li, J.; Zhang, Y.; Spratt, H.J.; Wang, H.; Will, G. Effects of metal ion concentration on electrodeposited CuZnSn film and its application in kesterite Cu_2ZnSnS_4 solar cells. *RSC Adv.* **2015**, *5*, 65114. [CrossRef]
65. Ozga, P.; Swiatek, Z.; Dębski, A.; Bonarski, J.; Tarkowski, L.; Bielanska, E.; Onderka, B.; Michalec, M. *Modern Technologies and Advanced Materials and Products in Balanced Development of Non-Ferrous Metals Industry*; IMN: Gliwice, Poland, 2010; Volume 295. (In Polish)
66. Trasatti, S. Work function; electronegativity, and electrochemical behaviour of metals. III. Electrolytic hydrogen evolution in acid solutions. *J. Electroanal. Chem.* **1972**, *39*, 163–184. [CrossRef]
67. Winiarski, J.; Tylus, W.; Krawczyk, M.S.; Szczygieł, B. The influence of molybdenum on the electrodeposition and properties of ternary Zn-Fe-Mo alloy coatings. *Electrochim. Acta* **2016**, *196*, 708–726. [CrossRef]
68. Khyzhun, O.Y.; Zaulychny, Y.V.; Zhurakovsky, E.A. Electronic structure of tungsten and molybdenum germanides synthesized at high pressures. *J. Alloys Compd.* **1996**, *244*, 107–112. [CrossRef]
69. Gassman, P.G.; Macomber, D.W.; Willging, S.M. Isolation and characterization of reactive intermediates and active catalysts in homogeneous catalysis. *J. Am. Chem. Soc.* **1985**, *107*, 2380–2388. [CrossRef]
70. Ng, K.T.; Hercules, D.M. Studies of nickel-tungsten-alumina catalysts by X-ray photoelectron spectroscopy. *J. Phys. Chem.* **1976**, *80*, 2094–2102. [CrossRef]

71. Clementi, E.; Raimondi, D.L.; Reinhardt, W.P. Atomic screening constants from SCF functions. II. Atoms with 37 to 86 electrons. *J. Chem. Phys.* **1967**, *47*, 1300–1307. [CrossRef]
72. Ramanauskas, R.; Gudavičiute, L.; Juškenas, R.; Ščit, O. Structural and corrosion characterization of pulse plated nanocrystalline zinc coatings. *Electrochim. Acta* **2007**, *53*, 1801–1810. [CrossRef]
73. Silva, A.M.N.; Kong, X.; Hider, R.C. Determination of the pKa value of the hydroxyl group in the α-hydroxycarboxylates citrate, malate and lactate by 13C NMR: Implications for metal coordination in biological systems. *BioMetals* **2009**, *22*, 771–778. [CrossRef]
74. Younes, O.; Gileadi, E. Electroplating of Ni/W Alloys. *J. Electrochem. Soc.* **2002**, *149*, C100–C111. [CrossRef]
75. Oue, S.; Nakano, H.; Kobayashi, S.; Fukushima, H. Structure and codeposition behavior of Ni–W alloys electrodeposited from ammoniacal citrate solutions. *J. Electrochem. Soc.* **2009**, *156*, D17–D22. [CrossRef]
76. Chassaing, E.; Quang, K.V.; Wiart, R. Mechanism of nickel-molybdenum alloy electrodeposition in citrate electrolytes. *J. Appl. Electrochem.* **1989**, *19*, 839–844. [CrossRef]
77. Gómez, E.; Pellicer, E.; Vallés, E. Detection and characterization of molybdenum oxides formed during the initial stages of cobalt-molybdenum electrodeposition. *J. Appl. Electrochem.* **2003**, *33*, 245–252. [CrossRef]